Chapter 1

Introduction to Fullerenes

1.1 Overview

Carbon-60, a hollow, all-carbon molecule [see Figure 1-1(c)], consists of sixty carbon atoms arranged at the vertices of a truncated icosahedron and joined with a mixture of single and double bonds. Its 12 pentagonal and 20 hexagonal faces form a symmetrical soccer-ball-like structure. Named for the American architect, inventor, and evangelist, R. Buckminster Fuller, who designed a geodesic dome with the same fundamental symmetry [4, 5], C_{60} molecules are called *buckminsterfullerenes* (or more affectionately, *buckyballs*).

Due to its all-carbon structure and extraordinarily high chemical and structural stability, C_{60} has often been referred to as the third major form of pure carbon, after diamond and graphite. Figure 1-2 shows the relationship between the crystal structure of these solids and the relative binding energies per carbon atom. All sixty carbon atoms comprising the C_{60} cage are equivalent, each sharing a double bond and two single bonds with its nearest neighbors. Since all bonds for each carbon atom are satisfied, pure C_{60} is expected to be either an insulator or a semiconductor.

Curiously, the original stimulus for the work that led to the discovery of C_{60} molecule [1] was an interest in certain unexplained features in the absorption and

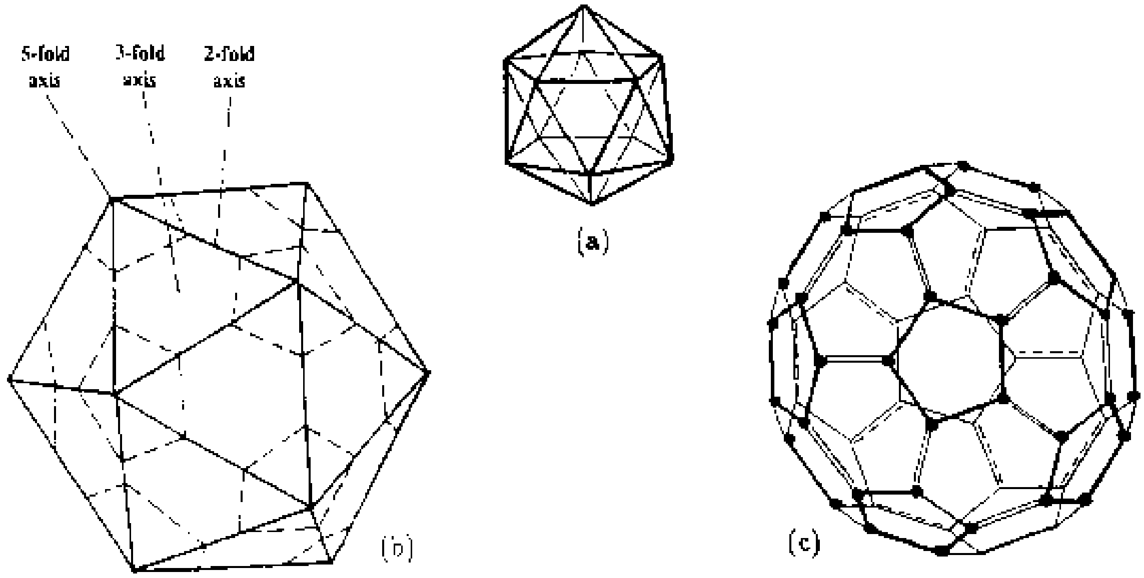

Figure 1-1: Icosahedral symmetry of C_{60}. (a) Icosahedron, one of the five Platonic solids. (b) Formation of a truncated icosahedron by cutting off the vertices of the icosahedron. Three types of symmetry axes of truncated icosahedron are indicated. (c) C_{60} molecule. All carbon atoms in C_{60} are equivalent, each sharing a double bond and two single bonds with its nearest neighbors. All bonds are satisfied, so that the chemical and structural stability of the molecule is very high.

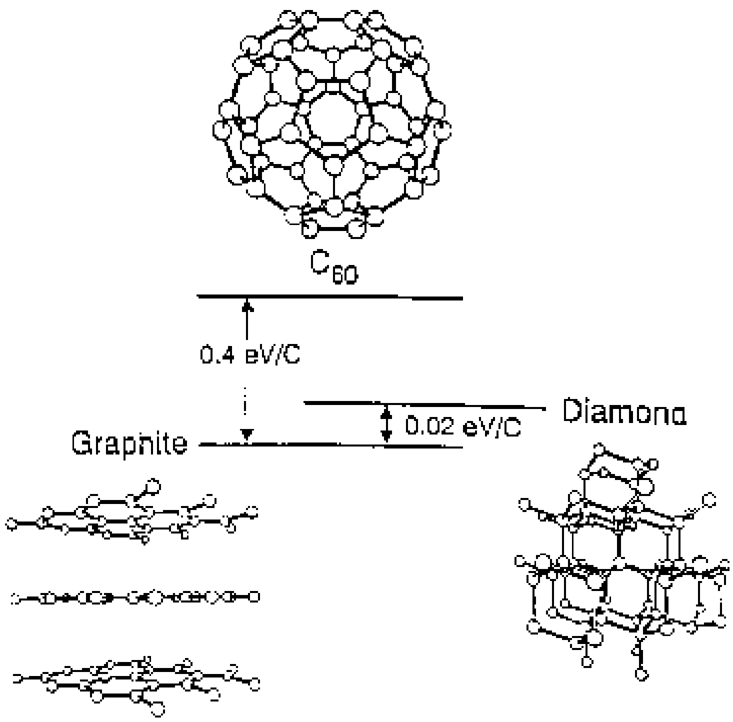

Figure 1-2: Schematic showing the relationship between the crystal structure of the three forms of carbon (graphite, diamond, and C_{60}) and their relative binding energies per carbon atom. Under normal conditions there are barriers present that prevent spontaneous conversion of C_{60} to diamond or graphite. (Adapted from Ref. [6].)

emission spectra of interstellar matter [7]. It has been proposed that C_{60} is indeed ubiquitous in the cosmos, and the special properties of C_{60} explain the observed spectral anomalies. Writes Harold Kroto, a co-discoverer of C_{60}:

> It is interesting to note that the motives for the experiments which serendipitously revealed the spontaneous creation and remarkable stability of C_{60} were astrophysical. Behind this goal lay a quest for an understanding of the curiously pivotal role that carbon plays in the origin of stars, planets, and biospheres. ... It is fascinating to now ponder over whether buckminsterfullerene is distributed throughout space, and we have not recognized it, and that it may have been under our noses on earth, or at least played an important role in some very common environmental processes, since time immemorial." [8]

It has also been suggested [9] that C_{60} may be responsible for the high abundance of certain elements in the Universe (notably, ^{22}Ne), and for the recently discovered [10] diamond-like domains in meteorites.

However, the first sighting of buckyballs in the wild happened here on Earth, and in the most unlikely place: Shunga, a Russian town in the lake region of Karelia, about 200 miles northeast of St. Petersburg. Peter Buseck *et al.* [11] discovered that a rock sample from Shunga they had been studying contained trace amounts of both C_{60} and C_{70}. Says Richard Smalley of Rice University, a co-discoverer of C_{60}: Next thing you know, they "might find a mine for buckyballs." [12]

In addition to C_{60}, many other closed-shell all-carbon molecules with different masses, *fullerenes*, have been observed. It has been shown [1, 13] that hollow three-dimensional carbon clusters with even numbers of carbon atoms (C_{2n} with $n > 15$) created, for instance, by laser vaporization of graphite, are fullerenes of various shape and stability (Fig. 1-3). Under most conditions, C_{60} is produced in noticeably greater yield that other C_{2n} clusters. The second most plentiful member of the fullerene family is C_{70}, a prolate-shaped molecule, which contains 10 additional carbon atoms

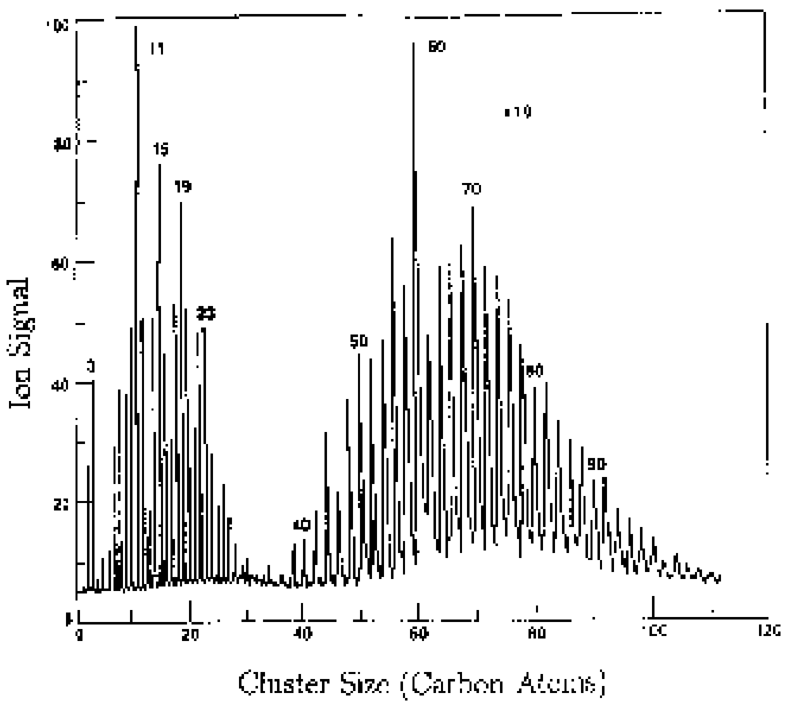

Figure 1-3: Time of flight mass spectrum of carbon clusters produced in a supersonic beam by laser vaporization of graphite [14].

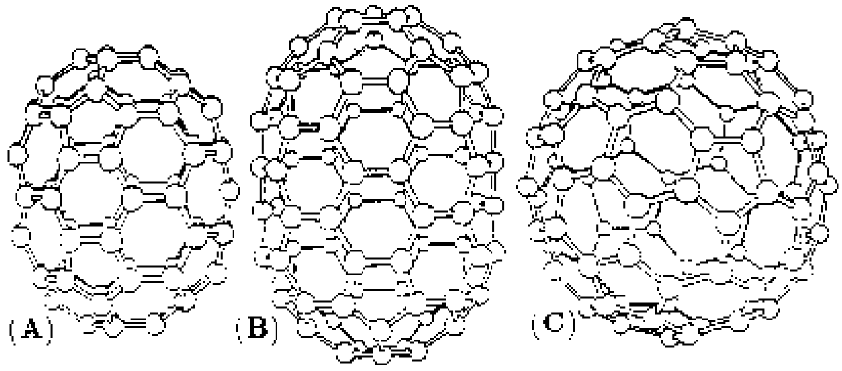

Figure 1-4: (**A**) C_{70} molecule as a rugby ball. (**B**) C_{80} molecule as an extended rugby ball. (**C**) C_{80} molecule as an icosahedron.

at the "equator" of the buckyball [Fig. 1-4(a).] Approximately 3–4% of a typical buckminsterfullerene output contains fullerenes larger than C_{60} and C_{70}. Some higher fullerenes [such as C_{80} on the Fig. 1-4(b,c)] can come in different shapes, forming isomers. Fullerenes consisting of as many as over a thousand carbon atoms have been observed. (See, for example, Curl and Smalley [15] for an overview of higher fullerenes and a variety of other fullerene structures.)

In addition to fullerenes, microtubules comprising coaxial tubes of graphite sheets terminated with fullerene end caps have been discovered [16] and dubbed *buckytubes* or *bucky fibers* (Fig. 1-5). Diameters on the order of tens of angstroms and lengths on the order of microns are typical, but recently, buckytubes with the diameter of a single C_{60} molecule have been synthesized [17, 18].

In this chapter, we shall briefly review the state of the art in the science of fullerenes. We shall start with an overview of synthesis (Sec 1.2) and an outline of molecular (Sec. 1.3.1) and crystalline (Sec. 1.3.2) structure of the fullerenes, concentrating on C_{60}, the most plentiful fullerene. The electronic structure of C_{60} molecules and solids will be briefly reviewed in Sec. 1.4. Various ways to introduce dopants into a C_{60} solid and the effects associated with doping (e.g., superconductivity) will be discussed in Sec. 1.5. In Sec. 1.6, a brief overview of the vibrational properties of

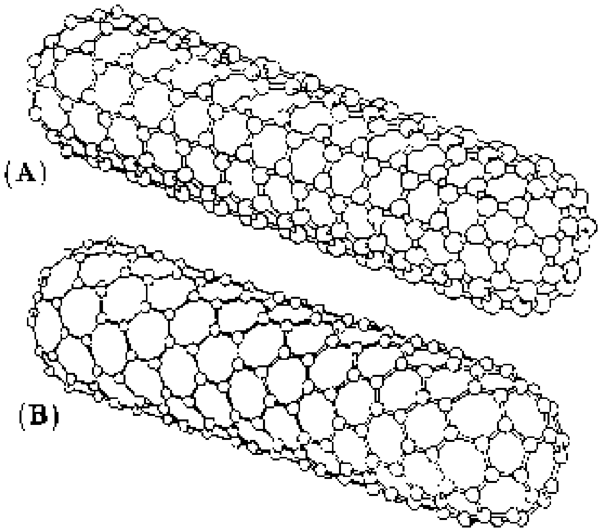

Figure 1-5: By rolling up a graphene sheet (a single layer from a 3-dimensional crystal of graphite) as a cylinder and capping each end of the cylinder with half of a C_{60} molecule, a "C_{60} tubule" one layer in thickness is formed. Shown here is a schematic model arising from: (**A**) an armchair cap with 5-fold axis, and (**B**) a zigzag cap with 3-fold axis. (Adapted from Ref. [19].)

C_{60} and C_{60}-based solids will be presented. We shall conclude with a brief outline of potential applications of the fullerenes (Sec. 1.7).

In the last few years, a number of thorough reviews on the subject of fullerenes have appeared [6, 15, 19–22], and a definitive book on fullerenes is about to be published [23]. It is not the aim of this overview to recount every conceivable property of the fullerenes that has ever been discovered. Instead, we shall mainly concentrate on those discoveries that are essential for understanding the structure and properties of the fullerenes and important to practical, in particular electronic, applications.

1.2 Synthesis

Although the fullerenes were discovered in 1985 [1, 14], and their unique structure received a good deal of attention in the scientific community at that time, experimental progress was hindered by the minuscule amounts produced in the gaseous residues of laser desorption experiments (see Fig. 1-3). This situation rapidly turned around in 1990 with the discovery by Krätschmer and Huffman of a simple and efficient technique to synthesize and concentrate macroscopic amounts of C_{60} and C_{70} [7]. A simplified schematic of their apparatus is presented on Fig. 1-6. The method is based on an AC arc discharge between graphite electrodes in approximately 200 Torr of He; the current can be supplied by a low-cost AC arc welder. The heat generated at the contact point between the electrodes evaporates carbon to form soot and fullerenes, which condense on the water-cooled walls of the reactor. Such an apparatus is capable of producing several grams of C_{60}/C_{70} per day. The discharge produces a carbon soot which can contain up to $\sim$15% of the fullerenes C_{60} ($\sim$13%) and C_{70} ($\sim$2%). Smaller fullerenes ($n \leq 84$ in C_n) are separated from the soot using Soxhlet extraction with a toluene solvent. The separation of C_{60} from C_{70} and the higher molecular weight fullerenes is typically accomplished using liquid chromatography.

For experiments where rigid exclusion of solvent impurities is necessary, it is pos-

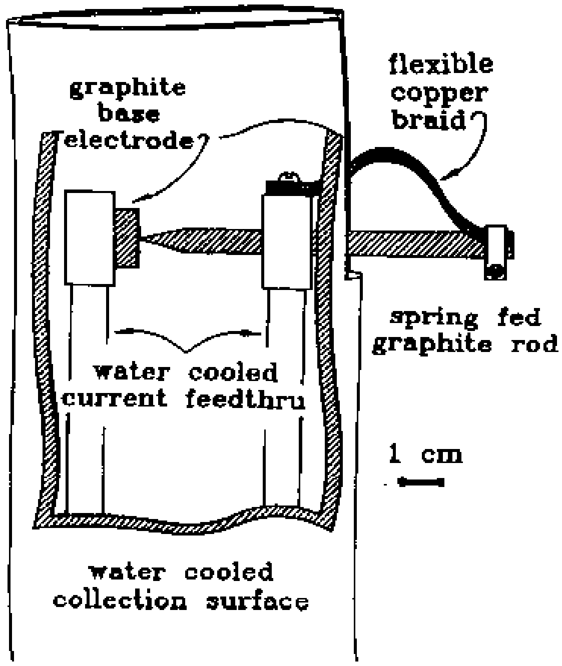

Figure 1-6: Schematic view of a simple contact-arc apparatus for the production of fullerene-rich soot.

sible to separate C_{60} and C_{70} from the arc-derived soot without the use of solvents by heating the soot in vacuum and in a temperature gradient. The C_{60} and C_{70} both are sublimed from the soot that is placed in the hottest part of the furnace and the fullerene molecules drift toward the cold end of a quartz tube connected to a vacuum line. The C_{60} and C_{70} molecules condense in separate bands on the tube wall, and the positions of these bands are related to different sublimation temperatures for C_{60} and C_{70}. For C_{60} or C_{70} powders obtained from liquid chromatography (LC), heat treatment in a dynamic vacuum of flowing inert gas (300°C for 1/2 to 1 day) is used to reduce the solvent impurity. Furthermore, solid C_{60} has been shown to intercalate or accept oxygen quite easily at 1 atm., particularly in the presence of visible or UV light. Thus, degassed powders should be stored in vacuum or in an inert gas (preferably in the dark).

Actual property measurements of fullerenes are made either on powder samples, films or single crystals. C_{60} powder is obtained from the solution which has passed through the LC column by vacuum evaporation of the solvent from the solution. Pristine C_{60} films can be deposited onto a substrate such as a clean silicon (100) or quartz surface by sublimation of the C_{60} powder in a vacuum of $\sim 10^{-6}$ Torr [7, 24]. Ellipsometry can be used to measure the thickness of the C_{60} films as they are deposited [25]. By variation of the substrate material and crystalline orientation, and by variation of the film growth temperature, the crystallite size and microstructure of the film can be varied. Single crystals can be grown either from solution using solvents such as CS_2, hexane and toluene or by vacuum sublimation [26]. The solution growth method tends to yield larger single crystals, but such crystals tend to contain trapped solvent. The smaller crystals ($\sim$0.5 mm in size) grown by sublimation (in vacuum or in an inert gas such as argon) tend to be more pure chemically and more perfect structurally.

1.3 Structure of Fullerenes

Prior to the discovery of the fullerenes [1], the only known forms of pure carbon were graphite and diamond (Sec. 1.1), both of which are *crystalline* materials. By contrast, the materials formed from fullerenes (called *fullerites*) are *molecular* solids, and their structure and properties are therefore strongly dependent on the structure and properties of the constituent fullerene molecules. The structure of the molecules is addressed below in Sec. 1.3.1, while the structure of fullerene molecular solids is reviewed in Sec. 1.3.2. This review is mainly limited to C_{60}, the most plentiful fullerene. While some information about the next most abundant fullerene, C_{70}, has been published, very little is known about higher fullerenes (C_{76}, C_{78}, C_{84}, etc.), and their practical importance is, therefore, very limited.

1.3.1 Molecular Structure of C_{60}

The sixty carbon atoms in C_{60} are located at the vertices of a regular truncated icosahedron where every site is equivalent to every other site [see Fig. 1-1(c)]. Since (1) the average nearest neighbor carbon-carbon (C–C) distance in C_{60} (1.44 Å) is almost identical to that in graphite (1.42 Å), (2) each carbon atom in graphite and in C_{60} is trigonally bonded to other carbon atoms and (3) most of the faces on the regular truncated icosahedron are hexagons, we can to a first approximation think of the C_{60} molecule as a "rolled-up" graphene sheet (a single layer of crystalline graphite) [19].

Like all polyhedra, the regular truncated icosahedron is subject to Euler's theorem:

$$f + v - e = 2 \tag{1.1}$$

where f, v, and e are, respectively, the number of faces, vertices, and edges of the polyhedron. Generally, for polyhedra formed by h hexagonal faces and p pentagonal faces, the total number of faces is

$$f = p + h \tag{1.2}$$

and, since each edge is shared by two faces, the total number of edges is

$$e = \frac{5p}{2} + \frac{6h}{2}. \tag{1.3}$$

By requiring that the polyhedron consist of only pentagons and hexagons, an additional constraint that each vertex is shared by three faces is introduced (note that the sum of the angles of faces adjacent to each vertex can not exceed 360°):

$$v = \frac{5p}{3} + \frac{6h}{3}. \tag{1.4}$$

From equations (1.2), (1.3), and (1.4), we easily derive that

$$f + v - e = \frac{p}{6},$$

which, by Euler's equation (1.2), yields

$$p = 12. \tag{1.5}$$

From this we conclude that all fullerenes with only hexagonal and pentagonal faces must have 12 pentagonal faces, and the number of hexagonal faces is arbitrary. In particular, the regular truncated icosahedron (C_{60}) has 20 hexagonal faces, in addition to its 12 pentagonal faces. Since the addition of a single hexagon adds two carbon atoms, all fullerenes must have an even number of carbon atoms, in agreement with the observed mass spectra for fullerenes as illustrated in Fig. 1-3.

The symmetry operations of the icosahedron consists of the identity operation, 12 five-fold axes through the centers of the pentagonal faces, 20 three-fold axes through the centers of the hexagonal faces, 15 two-fold axes through centers of the edges joining two hexagons [see Fig. 1-1(b)]. Each of the 60 rotational symmetry operations can be compounded with the inversion operation, resulting in 120 symmetry operations in the icosahedral point group I_h:

$$I_h = \{E, 12C_5, 12C_5^2, 20C_3, 15C_2\} \otimes i.$$

Molecules with I_h symmetry, of which C_{60} is the most prominent member, have the highest degree of symmetry of any known molecule.

The high aesthetic appeal of the buckyball has been linked to the famous golden ratio $\phi = \frac{1+\sqrt{5}}{2} \approx 1.61803$ prevalent in construction of the molecule (Fig. 1-7). Recently, the mathematics of the buckyball received great exposure in the works of Chung and Sternberg [28–30] and Bertram Kostant [31–33].

Although each carbon atom in C_{60} is equivalent to every other carbon atom, the three bonds emanating from each atom are not equivalent, two being electron-poor single bonds, and one being an electron-rich double bond (Fig. 1-1). This affects the length of the bonds making the single bonds around each pentagon longer than the double bonds at the edge of each pair of adjacent hexagons (see Table 1.1), which, however, preserves the icosahedral I_h symmetry of the molecule.

Table 1.1 summarizes some important physical constants for C_{60} molecules.

1.3.2 Crystalline Structure

Since each carbon atom has its valence requirements fully satisfied, the C_{60} molecules are expected to form a van der Waals bonded molecular solid which is either an insulator or a semiconductor (the band gap has been optically determined to be 1.7 eV [45]). The C_{60} molecules crystallize into a cubic structure with a lattice constant of 14.17 Å (see Table 1.2).

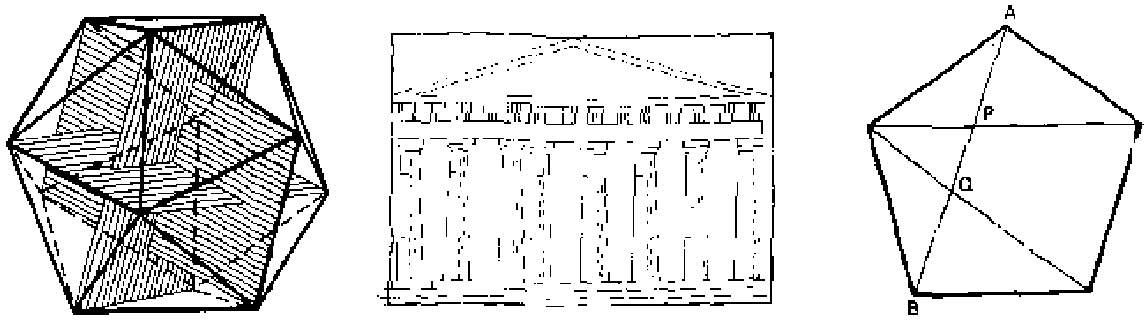

(a) (b) (c)

Figure 1-7: (a) *Regular icosahedron* is one of the five Platonic solids (polyhedra whose surface is bound by congruent regular polygons). Its twelve vertices can be divided into three coplanar groups of four. These lie at the corners of three golden rectangles which are mutually perpendicular and situated symmetrically with respect to each other, their common point being the centroid of the icosahedron. (b) A *golden rectangle* (a rectangle with sides of ratio ϕ) has been noted to have a particular aesthetic appeal. For example, the dimensions of The Parthenon at Athens (built in the fifth century B.C.), one of the world's most famous structures, can be fitted almost exactly into a golden rectangle. (c) Truncation of each vertex of an icosahedron [see Fig. 1-1(b)] results in 12 additional pentagonal faces being created. In each pentagon, the point of intersection (P or Q) of any two diagonals divides each in the golden ratio ϕ. The resulting solid, *truncated icosahedron*, maintains the high I_h symmetry of the regular icosahedron. (An excellent book by Huntley (Ref. [27]), from which figure (b) was taken, is full of fascinating facts about the golden ratio ϕ, with examples drawn from physics, mathematics, biology, architecture, and many other fields.)

Table 1.1: Physical constants for C_{60} molecules (after Ref. [23]).

Quantity	Value	Reference
Average C–C distance	1.44 Å	[34]
C–C bond length on a pentagon	1.46 Å	[35]
C–C bond length between adjacent hexagons	1.40 Å	[35]
C_{60} mean ball diameter[a]	7.10 Å	[36]
C_{60} ball outer diameter[b]	10.34 Å	–
Moment of inertia I	1.0×10^{-43}kg m^2	[37]
Volume per C_{60}	1.87×10^{-22}/cm^3	–
Number of distinct C sites	1	–
Number of distinct C–C bonds	2	–
Binding energy per atom	7.40 eV	[38]
Heat of formation (per g C atom)	10.16 kcal	[39]
Electron affinity	2.65$\pm$0.05 eV	[40]
Cohesive energy per C atom	1.4 eV/atom	[41]
Spin–orbit splitting of C($2p$)	0.00022 eV	[42]
First ionization potential	7.58 eV	[43]
Second ionization potential	11.5 eV	[44]
HOMO–LUMO gap	1.65 eV	[38]

[a] This value was obtained from NMR measurements. The calculated geometric value for the diameter is 7.09 Å (treating carbon atoms as mathematical points).
[b] This value for the outer diameter is found by assuming the thickness of the C_{60} shell to be 3.35 Å (taking account of the size of the π-electron cloud associated with the carbon atoms). In the solid, the C_{60}–C_{60} nearest-neighbor distance is 10.02 Å (see Table 1.2).

Table 1.2: Physical constants for crystalline C_{60} in the solid state (after Ref. [23]).

Quantity	Value	Reference
fcc Lattice constant	14.17 Å	[46]
C_{60}–C_{60} distance	10.02Å	[47]
C_{60}–C_{60} cohesive energy	1.6 eV	[48]
Tetrahedral interstitial site radius	1.12 Å	[47]
Octahedral interstitial site radius	2.07 Å	[47]
Mass density	1.72 g/cm^3	[47]
Molecular density	1.44 $\times 10^{21}$/cm^3	[47]
Compressibility ($-d\ln V/dP$)	6.9×10^{-12}cm^2/dyn	[49]
Bulk modulus[a]	14–18 GPa	[49–51]
Young's modulus[b]	15.9 GPa	[52]
Structural phase transition (T_{01})	261 K	[53]
dT_{01}/dp	11 K/kbar	[54, 55]
Vol. coeff. of thermal expansion	6.1×10^{-5}/K	[56]
Band gap (HOMO-LUMO)	1.7 eV	[45]
Velocity of sound v_t	2.1×10^5 cm/sec.	[52]
Velocity of sound v_l	3.6×10^5 cm/sec.	[52]
Debye temperature	185 K	[57, 58]
Thermal conductivity (300 K)	0.4 W/mK	[59]
Electrical conductivity (300 K)	1.7×10^{-7} S/cm	[60]
Phonon mean free path	50 Å	[59]
Static dielectric constant	4.0 – 4.5	[24, 25, 61]
Melting temperature	1180°C	[62]
Sublimation temperature	~350°C	[63]
Heat of sublimation	40.1 kcal/mol	[64]
Latent heat	1.65 eV	[65]

[a]Recently, the bulk modulus at room temperature of 6.8 GPa in the fcc phase and 8.8 GPa in the sc phase below T_{01} has been reported [66]. The conversion of units for pressure measurements is 1 GPa $= 10^9$ N/m^2 $= 0.99$ kbar $= 7.52\times10^6$ torr $= 10^{10}$ dyn/cm^2. Also, 1 atm = 760 torr $= 1.01\times10^5$ Pa.
[b]For solvated C_{60} crystals measured by vibrating reed method [52]. Measurements on film samples suggest a higher Young's modulus [67].

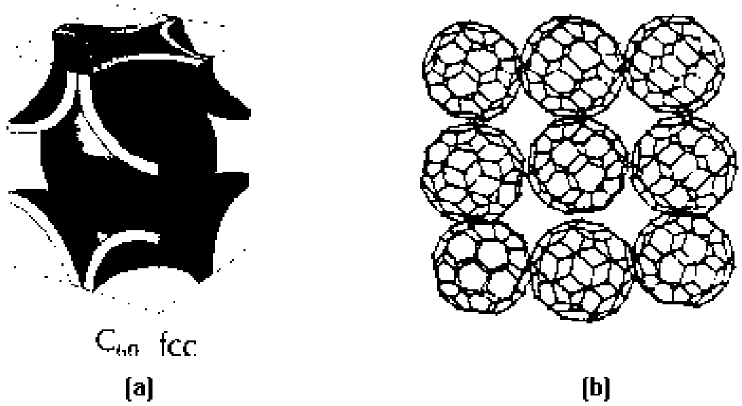

Figure 1-8: (a) A bct unit cell illustrating the fcc structure of C_{60} crystalline solid at $T > 255$ K. The buckyballs are rotating rapidly with three degrees of rotational freedom, rendering all balls equivalent on average (on the time scale greater than one over the frequency of rotation). (b) C_{60} solid at low temperatures: the buckyballs are frozen in inequivalent positions in a simple cubic lattice [68].

Structural phase transition

At room temperature, the balls are rotating rapidly with three degrees of rotational freedom, and the ball centers are arranged on a face centered cubic (fcc) lattice (space group O_h^5 or $Fm\overline{3}m$) with one C_{60} ball per primitive fcc unit cell, or 4 balls per simple cubic unit cell [see Fig. 1-8(a)].

Below the structural phase transition $T_{01} \approx 260$ K, the C_{60} balls completely lose two of their 3 degrees of rotational freedom, and the residual *hindered* rotational motion occurs only along the four $\langle 111 \rangle$ axes. The structure of solid C_{60} below $\sim$260 K thus becomes simple cubic (space group T_h^6 or $Pa\overline{3}$) with a lattice constant $a_0 =$ 14.17 Å and four C_{60} molecules per unit cell, as the four balls within the fcc structure become inequivalent [Fig. 1-8(b)]. The reason for this transition lies in the fact that, at temperatures below 260 K, adjacent C_{60} molecules develop correlated orientations. The lowest energy is achieved when an electron-rich double bond of one C_{60} molecule is aligned with the electron-poor pentagonal face of an adjacent C_{60} ball [Fig. 1-

Figure 1-9: Electron-rich double bond on one C_{60} molecule (shaded) opposite an electron-poor (a) pentagonal face and (b) hexagonal face of the adjacent molecule (not shaded).

9(a)]. Another structure with only slightly higher energy places the electron-rich double bond of one C_{60} molecule opposite an electron-poor hexagonal face [see Fig. 1-9(b)]. (Predictably, as the temperature T is lowered below 260 K, the probability of occupying the lower energy configuration increases [69].) A mixture of these alignment configurations in the fullerene solid is achieved by the ratcheting motion of the C_{60} molecules around the $\langle 111 \rangle$ axes as they execute a hindered rotational motion. The ratcheting motion begins below the 250 K phase transition and continues down to low temperatures, but the residual structural disorder has been shown to persist to temperatures as low as 5 K [69].

The 260 K phase transition affects almost all properties of the C_{60} solid, and it has been observed in differential scanning calorimetry [70], specific heat [58] (Fig. 1-10), resistivity [71], NMR [36, 70, 72, 73], ultrasonic attenuation [52], Raman spectroscopy [74], thermal conductivity [59], and the thermal coefficient of the lattice expansion [56] (Fig. 1-11). The effects of this phase transition on the measured transport and dielectric properties of C_{60} films are discussed in Sections 4.4.2 and 4.8, respectively.

Second-order phase transition

Evidence for a second phase transition at $T_{02} \sim 165$ K is provided by ultrasonic attenuation studies [52], specific heat measurements [58, 75] (Fig. 1-10), dielectric relaxation

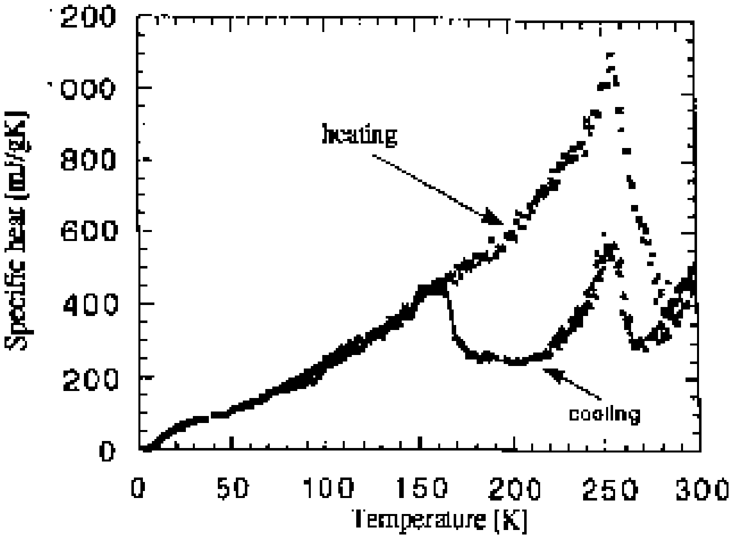

Figure 1-10: Comparison between the temperature dependence of the specific heat for C_{60} on cooling (Δ) and heating ($\times$) [58].

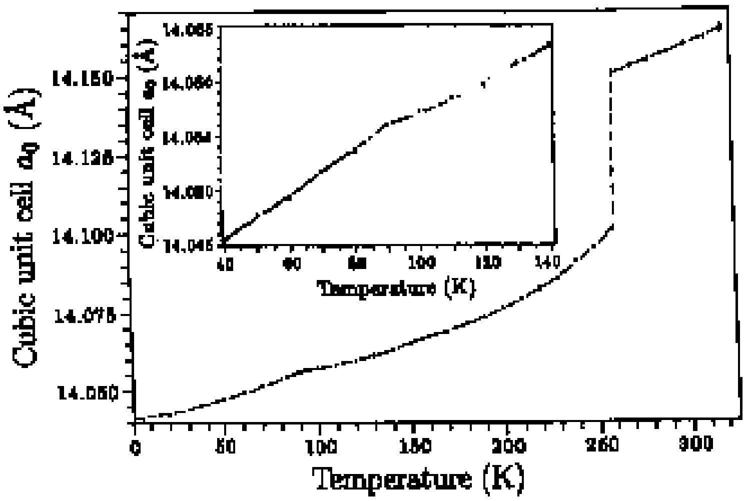

Figure 1-11: Temperature variation of the cubic lattice constant a_0 for solid C_{60}. The inset shows the low temperature data for a_0 on an expanded scale. [56]

studies [76], electron microscopy observations [77], neutron scattering measurements [69] and Raman scattering studies [74].

In contrast to the $T_{01} = 260$ K structural phase transition, which is sensitively studied by static diffraction techniques, the phase transition occurring near 165 K is most sensitive to dynamic processes, such as the frequency dependence of the dielectric response function [76], ultrasonic attenuation [52], and dynamic NMR processes [36]. Characteristic of the behavior of a *glassy* phase transition, the transition temperature T_{02} is not fixed, but is a function of the temperature scanning rate of the probe [69, 76], its value varying by as much as 20 K.

The ratcheting motion described above allows a greater fraction of the C_{60} molecules to align so that the electron-rich double bonds are opposite the electron-poor pentagons as the temperature is decreased. By $T = 90$ K, $\sim$83% of the inter-molecular alignments are reported to be in the lower energy state, leaving $\sim$17% in the higher energy state where the double bond of one molecule is opposite a hexagonal face on the adjacent molecule [69]. Below 90 K, the ratcheting motion continues down to about 50 K, but in this regime, the same fraction ($\sim$83% and $\sim$17%) of the relative intermolecular orientations is maintained and the ratcheting motion is from one orientation to an equivalent orientation. The random occurrence of the higher energy alignment state gives rise to a disordered two-state tunneling system which has been studied by both specific heat [75] and thermal conductivity [59] measurements.

Photopolymerization

It has recently been shown [45] that, under laser or UV irradiation, the C_{60} molecules cross-link to form multi-ball polymers (mostly dimers). The figure 1-12 shows the laser desorption mass spectra for the pristine (a) and phototransformed (b) C_{60} films [45, 78]. The peaks in (a) are identified with clusters of cross-linked fullerene molecules. Clearly, the phototransformation process creates mostly dimers (C_{120}), a substantial amount of trimers (C_{180}), as well as other oligomers $(C_{60})_n$.

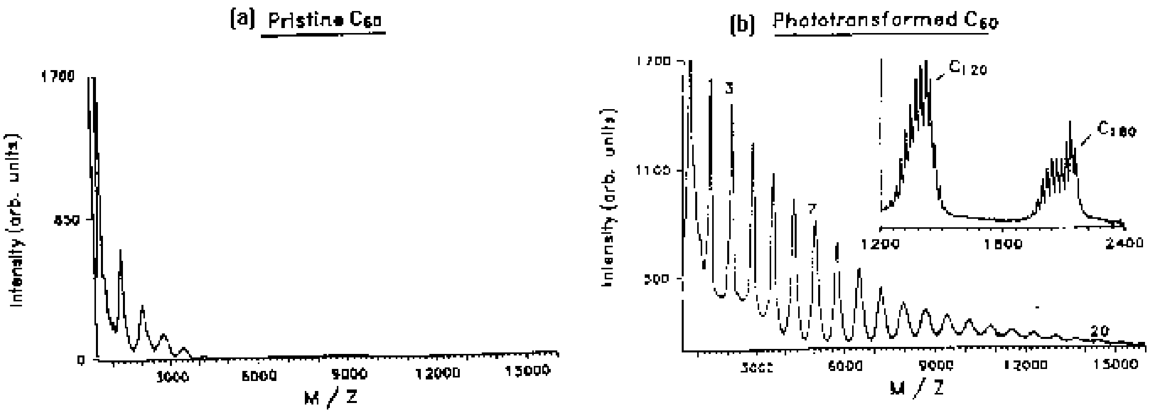

Figure 1-12: (a) Laser desorption mass spectrum (LDMS) for pristine C_{60} films (laser desorption fluence is 30 mJ$\cdot$cm^{-2}). The spectrum indicates the presence of $(C_{60})_n$ clusters, $n < 4$. These peaks are identified with cross-linked C_{60} molecules produced by the desorption laser itself. (b) LDMS spectrum of a phototransformed C_{60} film. A succession of 20 clear peaks identified with large clusters of fullerene molecules $(C_{60})_n$ $(0 \leq n \leq 20)$ is observed in the spectrum. Inset demonstrates, on an expanded scale, the fine structure of the $n = 2$ and $n = 3$ peaks associated with C_2 loss and gain from the clusters in the desorption process [45, 78].

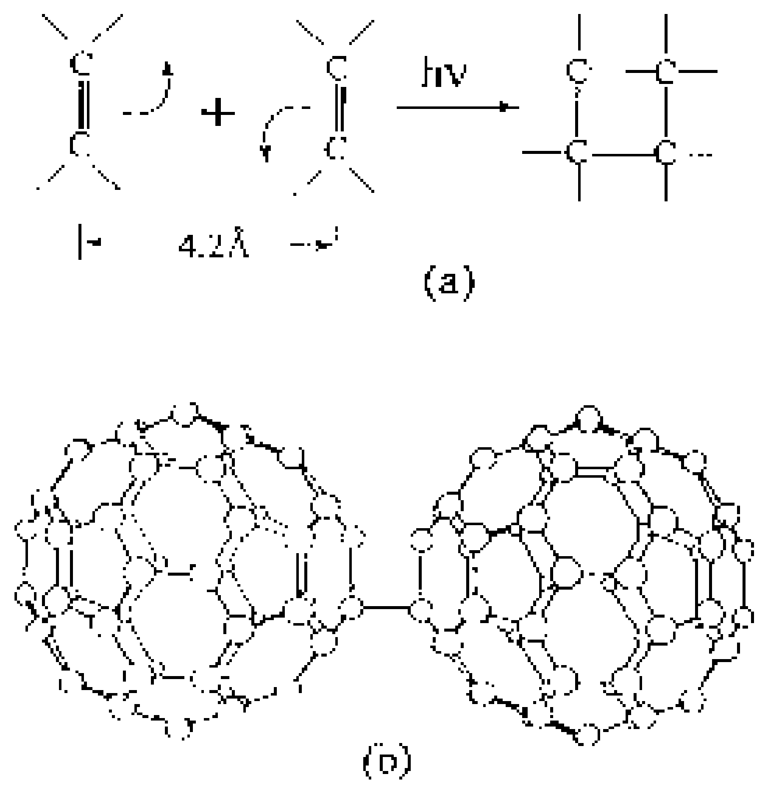

Figure 1-13: (a) A schematic of the photon-assisted 2+2 cycloaddition reaction between parallel carbon double bonds of adjacent C_{60} molecules. (b) A C_{60} dimer (C_{120}) produced by the photochemical reaction (a).

The evidence to date (AFM, SEM, HRTEM, X-rays, Raman, solubility and other physical property changes) suggests that the dimers are formed by light-induced 2+2 cycloaddition reaction between two buckyballs, which creates two covalent bonds between the fullerene shells (see Fig. 1-13). This structure has also been shown to be the one of lowest energy among all available dimer structures by, e.g., generalized tight-binding [79] and first principles [80] molecular dynamics calculations.

In addition to significantly affecting physical properties (optical and vibrational properties, solubility, high resistance to thermal sublimation) of the C_{60} crystalline solids, the photopolymerization reaction also causes marked structural changes. The cross-linking reduces the inter-ball separation in the solid, which results in a $\sim$5%

reduction of the lattice constant. This "shrinkage" has been confirmed by X-ray diffraction [81], by high resolution transmission electron microscopy (HRTEM, see Fig. 1-14), and by observing cracks in the surface layer of C_{60} films [45] and crystals [82] subjected to high intensity vis-UV illumination.

In order for the 2+2 cycloaddition mechanism to work, the adjacent C_{60} molecules must be able to align such that their double bonds are located in close proximity (Fig. 1-13). At $T > T_{01}$, when all molecules are spinning freely about their equilibrium fcc lattice locations, such alignment is very likely, as the molecules can adopt 30(30)=900 favorable orientations promoting the 2+2 cycloaddition. However, below the structural transition temperature ($T < T_{01}$), the molecules' orientations "freeze out," and alignment and cycloaddition are no longer observed [83]. A recent review [84] discusses photochemical transformations of the fullerenes in much detail.

1.4 Electronic Structure

On the basis of the spectroscopic studies (Sec. 1.6), it has been concluded that the fullerenes form molecular solids. Thus, their electronic structures are expected to be closely related to the electronic levels of the isolated molecules. Each carbon atom in C_{60} has two single bonds along adjacent sides of a pentagon and one double bond between two adjoining hexagons. If these bonds were coplanar, they would be very similar to the sp^2 trigonal bonding in graphite. The curvature of the C_{60} surface causes the planar-derived trigonal orbitals to hybridize, thereby admixing some sp^3 character to the sp^2 bonding. The shortening of the double bonds and lengthening of the single bonds also strongly influence the electronic structure.

Figure 1-15(a) displays the results of a Hückel energy calculation for an isolated C_{60} molecule. Because of the molecular nature of solid C_{60}, the electronic structure for the solid phase would be expected to be closely related to that of the free molecule. Indeed, the relatively small ($\sim$0.4 eV) dispersion of the bands derived from the h_u

Figure 1-14: High resolution transmission electron microscopy (HRTEM) photograph of a C_{60} crystallite before (a) and after (b) photopolymerization in a 488 nm Argon-ion laser. The C_{60} film has been deposited on a carbon film TEM substrate as described in Sec. 4.5. A $\sim$5% reduction in the lattice constant after polymerization has been demonstrated by Fourier transform image analysis. Note also that the microstructure of the film is considerably more disordered after photopolymerization, with long range ordering largely destroyed by exposure to light.

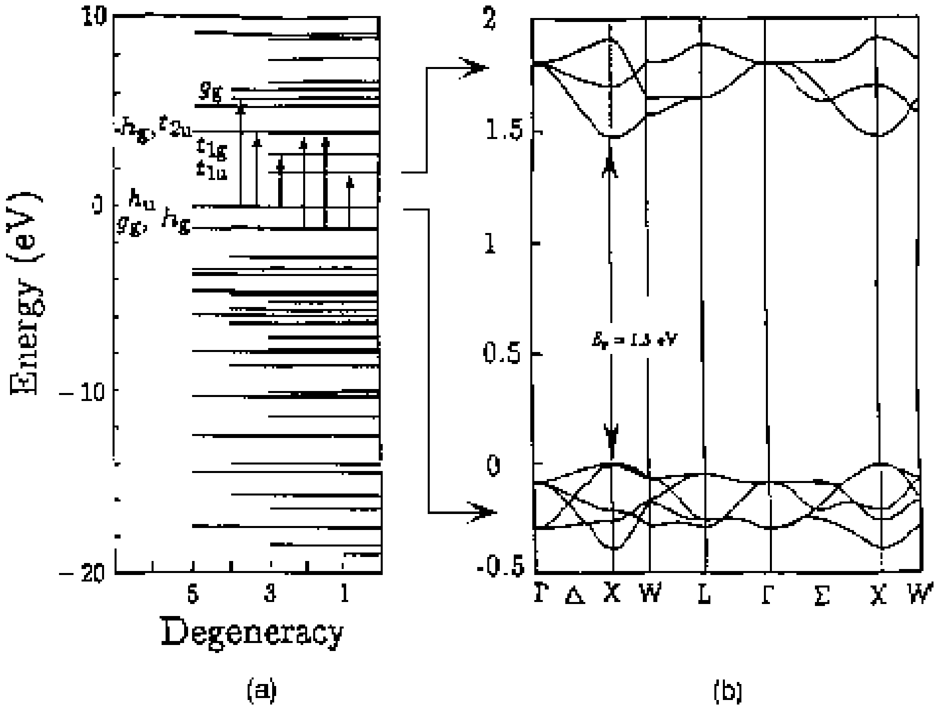

Figure 1-15: (a) Calculated electronic structure of an isolated C_{60} molecule. The allowed dipole transitions are indicated by arrows. (b) Local density approximation calculations for fcc solid C_{60} show energy dispersion of the five h_u-derived valence bands and the three t_{1u}-derived conduction bands. The direct gap at the X point is calculated to be 1.5 eV. The bands are relatively narrow (~0.4 eV), and the electronic structure of the solid strongly reflects the molecular character of the isolated molecule [85].

(HOMO) and t_{1u} (LUMO) levels, as calculated by the local density approximation, [see Fig. 1-15(b)] supports this conclusion.

1.5 Doping

As was pointed out above, all bonding requirement of the constituent carbon atoms of a C_{60} molecule are satisfied, and pristine C_{60} forms an insulator with a HOMO-LUMO band gap[1] of 1.7 eV [45]. However, by introducing various dopants into the large intersticial spaces of fullerenes, their properties can be modified dramatically in scientifically interesting and practically important ways. In particular, depending on the doping and processing, fullerene solids can be insulators, semiconductors, conductors, or superconductors, spanning the entire spectrum of electrical properties.

The four distinct ways to introduce foreign atoms into a C_{60}-based solid are reviewed below [86].

Endohedral Doping

One doping method is the addition of a rare earth, an alkaline earth or an alkali metal ion into the interior of the C_{60} ball to form an endohedrally doped molecular unit [Fig. 1-16(a)]. This configuration has, for example, been denoted by La@C_{60} for one endohedral lanthanum in C_{60}, or Y_2@C_{82} for two Y atoms inside a C_{82} fullerene [87]. The endohedral dopants of C_{60} confirmed to date include Ca, Co, Cs, Fe, He, K, La, La_2, Mu, Ne, Rb, U, U_2, and Y_2 [23].

Thus far, only very small quantities of endohedrally doped fullerenes have been prepared and their study has been limited to investigations of isolated endohedrally doped fullerenes. No studies of crystalline material composed of endohedrally doped constituents have yet been reported.

[1] Strictly speaking, this value refers to the optical absorption edge rather than to the HOMO-LUMO band gap. The value of 1.7 eV does not take into account the exciton binding energy.

Since the dopant atom (or atoms) is usually positioned asymmetrically inside the carbon cage of a fullerene, creating a permanent electric dipole, endohedral fullerene solids are expected to have very interesting dielectric properties. The heavier endohedral dopants may give rise to fullerene materials exhibiting high dielectric constants extending down to the practically important low frequency regimes. (For a review of the dielectric properties of fullerenes, see Chapter 4.)

Substitutional Doping

A second doping method is the substitution of an impurity atom with a different valence state for a carbon atom on the surface of a C_{60} ball. Since a carbon atom is so small, and since the average nearest-neighbor C–C distance on the C_{60} surface is only 1.44 Å, the only species that can be expected to substitute for a carbon atom on the C_{60} ball surface are boron and nitrogen. Boron induces an acceptor state making the charged ball p-type, whereas nitrogen induces a donor state, yielding an n-type material [88]. Smalley and coworkers have demonstrated that it is possible to replace more than one carbon atom by boron on a given ball [86]. A few groups have also reported detection of nitrogen-substituted fullerenes [89–91].

Radial Exohedral Doping

Dopants to fullerenes have also been added via radial bonds to the outside of C_{60} balls. Two examples of such radial exohedral doping have been observed for fluorine and hydrogen doping. In the case of radial exohedral fluorine doping, the attachment of an F atom converts a double bond in C_{60} into a single bond [92]. A report has been given of adding up to 60 fluorine atoms per ball, to form $C_{60}F_{60}$ [Fig. 1-16(b)] where all double bonds on the C_{60} molecule have been converted to single bonds [93]. However most authors report lower fluorine doping levels. Similar bonding arrangements of C_{60} to hydrogen have also been reported up to a maximum hydrogen concentration, $C_{60}H_{60}$ [94]. However, it is not known whether in the case of $C_{60}H_{60}$ all the H-bonds

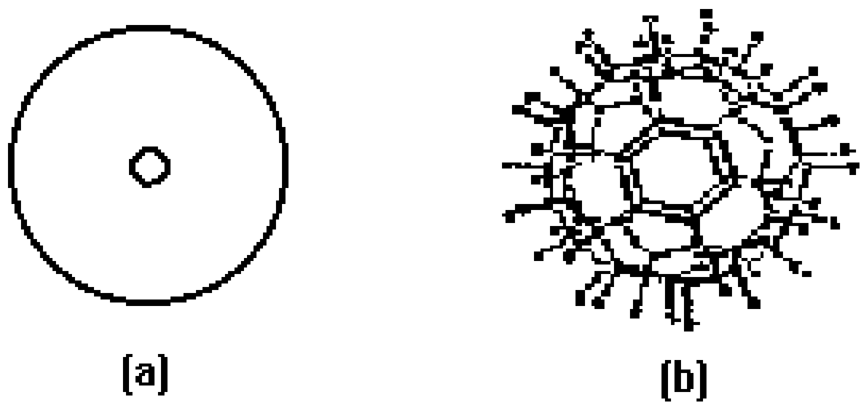

Figure 1-16: (a) Endohedrally doped La@C_{60} fullerene. (b) Proposed structure for fully fluorinated buckyball, $C_{60}F_{60}$ [93].

are directed radially outward, or whether some may perhaps be directed radially inward and be endohedrally bonded [87]. A variety of bromine [95], and chlorine [96] doped fullerenes have also been prepared, though the doping arrangement in the case of bromine and chlorine may well be different from that for fluorine and hydrogen.

Exohedral Donor Doping

The most common method of doping fullerene solids is exohedral donor doping (also called intercalation). In this case, the dopant (e.g., an alkali metal M) is introduced into the interstitial positions between adjacent balls (exohedral locations) [97]. Charge transfer can take place between the M atoms and the balls, so that the M atoms become positively charged ions and the balls become negatively charged with predominately delocalized electrons.

Among the alkali metals, Li, Na, K, Rb, and Cs have all been used as exohedral dopants for C_{60}, as well as intermetallic mixtures of these alkali metals such as Na_2K and Rb_xCs_y. Figure 1-17 illustrates the evolution of structure of the fullerene solid as the fcc C_{60} crystal is intercalated with alkali metal atoms.

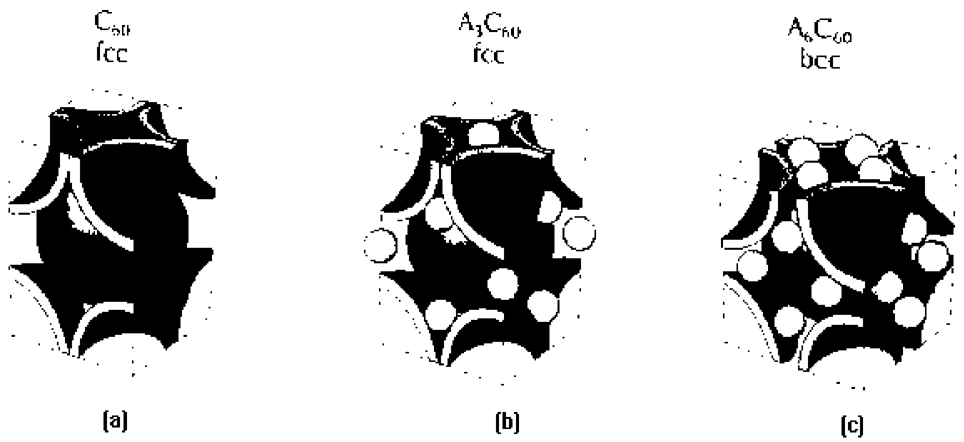

Figure 1-17: Structures for solid (a) C_{60}, (b) M_3C_{60}, (c) M_6C_{60} (M=K,Rb). The large balls denote C_{60} molecules, and the small balls are alkali metal ions. For fcc M_3C_{60} (b), which has four C_{60} balls per cubic unit cell, the M atoms can either be on octahedral or tetrahedral sites. Undoped solid C_{60} also exhibits this crystal structure, but in this case all tetrahedral and octahedral sites are unoccupied. For bcc M_6C_{60} (c) all the M atoms are on distorted tetrahedral sites. (Adapted from Ref. [98].)

While the electrical resistivity ρ of pristine C_{60} is relatively high (see Table 1.2), it can be decreased by several orders of magnitude by doping with alkali metals, which create carriers at the Fermi level. As x in M_xC_{60} increases, the resistivity ρ approaches a minimum at $x = 3.0 \pm 0.05$ [97], corresponding to a half-filled conduction band. Then, upon further increase in x from 3 to 6, ρ again increases, as is shown in Fig. 1-18(a) [99].

Perhaps the most striking property of the C_{60}-related materials is the observation of high temperature superconductivity [see Fig. 1-18(b)]. The early observation of superconductivity at 18 K in K_3C_{60} [100] was soon followed by observations of superconductivity at even higher temperatures: in Rb_3C_{60} (T_c = 30 K) [101, 102], $Rb_xCs_yC_{60}$ (T_c = 33 K) [103], and, most recently, Cs_3C_{60} (T_c = 40 K, under pressure) [104]. This large increase in T_c was achieved in going to compounds with larger intercalate atoms resulting in unit cells of larger size and with larger lattice constants (see Fig. 1-19). As the lattice constant increases, the ball-ball coupling decreases,

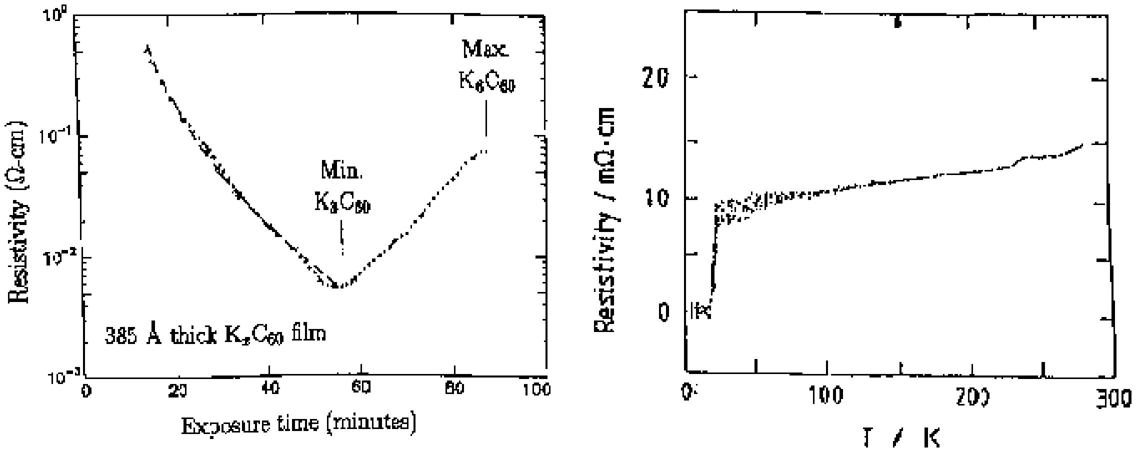

Figure 1-18: (a) Dependence of the resistivity (logarithmic scale) of a K_xC_{60} film on exposure to K vapor at ambient temperature near 70°C. The dashed curve is a fit to theory that treats the conductivity as an activated process with an activation energy derived from charging energies of individual K_3C_{60} grains (adapted from Ref. [99]). (b) Superconducting transition at T_c=18 K and temperature dependence of the resistivity ρ of single crystal K_3C_{60} showing a nearly linear increase in ρ above T_c. Note the anomaly in $\rho(T)$ at $T = T_{01} \approx 260$ K due to the structural transition.

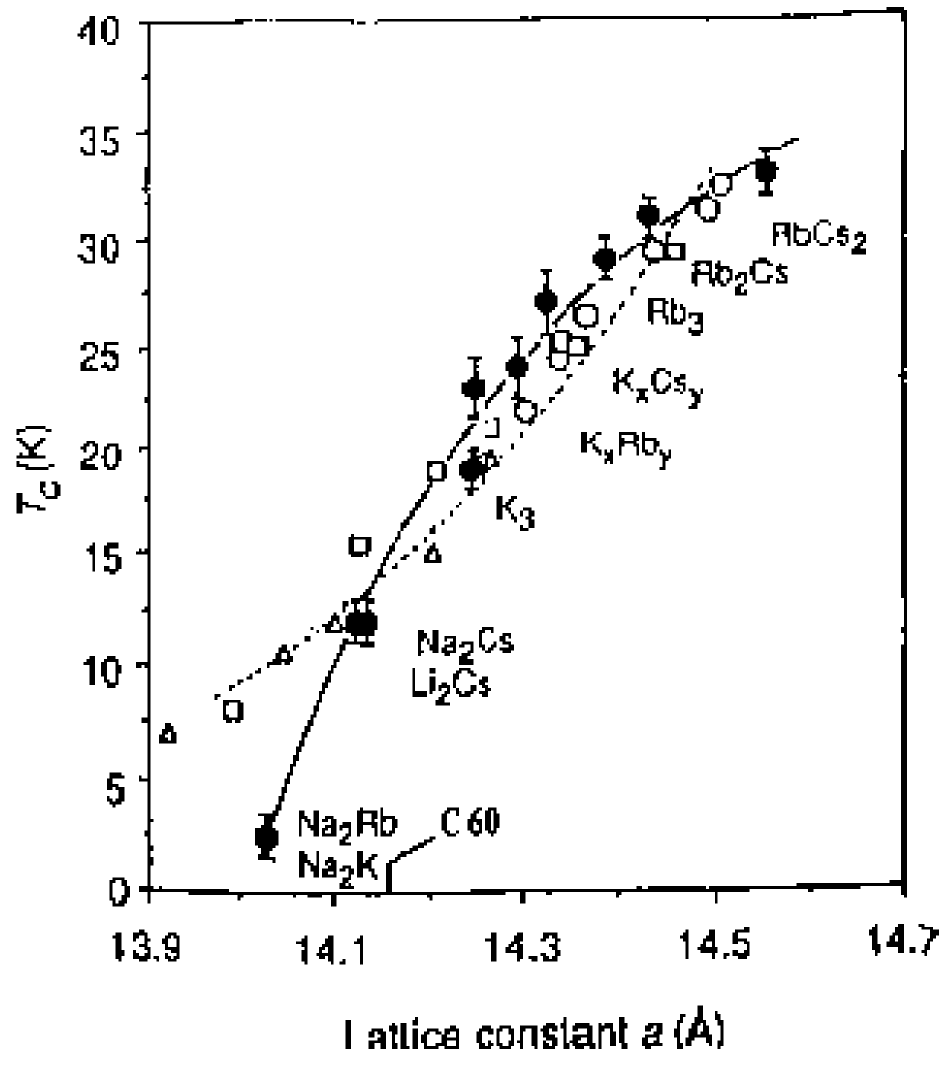

Figure 1-19: Dependence of T_c on the lattice constant a for various M_3C_{60} compounds (M=Li,Na,K,Rb,Cs) [98]. Note the almost linear relation between T_c and a for compounds with a greater than that for undoped C_{60} (M=K,Rb,Cs). [Note that this holds true for both ambient pressure (solid points) and high pressure (open points) results.] On the other hand, for the compounds intercalated with Li and Na, a falls below that for C_{60} itself, and the correlation between T_c and a breaks down because of the attractive electrostatic interaction introduced by the presence of the alkali metal ions in the lattice, and because of different rotational disorder.

narrowing the bandwidth of the LUMO-derived level, and thereby increasing the corresponding density of states at the Fermi level $N(E_F)$. Thus, the increase in T_c is consistent with the BCS expression relating the transition temperature to the density of states $N(E_F)$:

$$T_c \sim \omega_{ph} \exp\left(-\frac{1}{VN(E_F)}\right), \tag{1.6}$$

where V is the electron-phonon coupling energy.

While the crystalline phases formed by intercalation of alkali metals have been the ones most widely studied (because of their superconducting properties), some structural reports have been given for fullerene-derived crystals with alkaline earth [46] and iodine [105] intercalants.

A completely different type of exohedral intercalant of crystalline C_{60} is molecular oxygen (O_2), as well as some other gases (notably, NO). These intercalants also alter the properties of fullerites dramatically (in particular, transport, photoelectric, and dielectric properties), and their effect is discussed in Section 4.4.1.

1.6 Vibrational Properties

The normal modes for solid C_{60} can be clearly subdivided into two main categories: "intramolecular" and "intermolecular" modes, because of the apparent weak coupling between molecules. The former are often simply called "molecular" modes, since their frequencies and eigenvectors closely resemble those of an isolated molecule. The latter are also called lattice modes, and can be further subdivided into librational, acoustic and optic modes. All of these modes, except the acoustic lattice modes, appear schematically in Fig. 1-20 [106].

Because of the high symmetry of the C_{60} molecule (point group I_h), there are only 46 distinct molecular mode frequencies corresponding to the $180 - 6 = 174$ degrees of freedom for the isolated C_{60} molecule, and of these only 4 are infrared-active (all with T_{1u} symmetry) and 10 are Raman-active (2 with A_g symmetry and 8

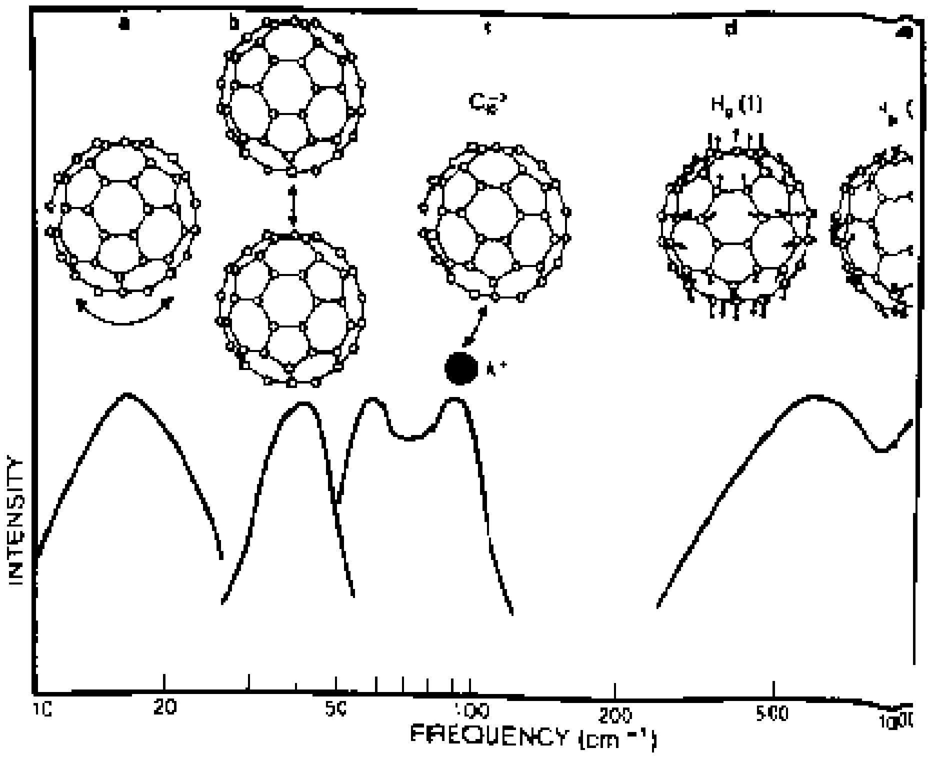

Figure 1-20: Various vibrations in the M_3C_{60} compounds. At lower energies the compounds exhibit librational modes of individual C_{60} molecules (a), inter-ball optic modes (b), and ball–alkali metal (see Sec. 1.5) optic modes (c). The schematic density of states shown for these modes represents a true continuum, which is found throughout the entire Brillouin zone. At higher energies the intramolecular modes dominate; these "on-ball" modes have a radial character (d) at lesser energies [for example the $H_g(1)$ mode] and a tangential character (e) at higher energies [for example, the $H_g(7)$ mode]. The arrows indicate the C-atom displacements in each mode. The schematic density of states for the intra-molecular vibrations exhibits two broad peaks, with the lower and upper peaks associated, respectively, with the modes having predominantly radial and tangential molecular displacements [106].

with H_g symmetry). The remaining 32 eigenfrequencies correspond to silent modes (Table 1.3).

Raman and infrared spectroscopy provide sensitive methods for distinguishing C_{60} from higher molecular weight fullerenes and modified [photopolymerized (Sec. 1.3.2) or doped (Sec. 1.5)] fullerene solids. Since most of the higher molecular weight fullerenes have lower symmetry as well as more degrees of freedom, they have many more infrared- and Raman-active modes. Figure 1-21 illustrates this by comparing the Raman and IR spectra of fullerene films before and after polymerization.

The vibrational properties of C_{60} and other fullerenes have been modeled with a variety of force-constant [110, 111] and first principles calculations [79, 80]. We have also conducted a classical molecular dynamics study of the vibration properties of C_{60} and photopolymerized C_{60}, but the discussion of results of this study is well beyond the scope of this thesis (see Sec. 5.3).

1.7 Applications†

Although research on solid C_{60} and related materials is still at an early stage, these materials are already beginning to show many exceptional properties, some of which may lead to practical applications. Small-scale applications will come first; then targeted applications utilizing the special properties of fullerenes are expected to follow.

In this section, we shall concentrate on those applications pertaining to novel fullerene-based electronic devices. An all-inclusive discusion of various applications of the fullerenes can be found in the Chapter 20 of Ref. [23].

†This section closely follows Chapter 20 of the Ref. [23].

Table 1.3: Experimental values for the intramolecular vibrational frequencies of the C_{60} molecule and their symmetries. The frequencies are derived from a fit to first-order and higher-order Raman [107] and IR spectra [108]. The Raman-active modes have A_g and H_g symmetry and the IR-active modes have F_{1u} symmetries. The remaining 32 modes are refereed to as silent modes.

Even-parity		Odd-parity	
$\omega_i(\mathcal{R})$	Frequency (cm^{-1})	$\omega_i(\mathcal{R})$	Frequency (cm^{-1})
$\omega_1(A_g)$	497.5	$\omega_1(A_u)$	1143.0
$\omega_2(A_g)$	1470.0		
		$\omega_1(F_{1u})$	526.5
$\omega_1(F_{1g})$	502.0	$\omega_2(F_{1u})$	575.8
$\omega_2(F_{1g})$	975.5	$\omega_3(F_{1u})$	1182.9
$\omega_3(F_{1g})$	1357.5	$\omega_4(F_{1u})$	1429.2
$\omega_1(F_{2g})$	566.5	$\omega_1(F_{2u})$	355.5
$\omega_2(F_{2g})$	865.0	$\omega_2(F_{2u})$	680.0
$\omega_3(F_{2g})$	914.0	$\omega_3(F_{2u})$	1026.0
$\omega_4(F_{2g})$	1360.0	$\omega_4(F_{2u})$	1201.0
		$\omega_5(F_{2u})$	1576.5
$\omega_1(G_g)$	486.0		
$\omega_2(G_g)$	621.0	$\omega_1(G_u)$	399.5
$\omega_3(G_g)$	806.0	$\omega_2(G_u)$	760.0
$\omega_4(G_g)$	1075.5	$\omega_3(G_u)$	924.0
$\omega_5(G_g)$	1356.0	$\omega_4(G_u)$	970.0
$\omega_6(G_g)$	1524.5†	$\omega_5(G_u)$	1310.0
		$\omega_6(G_u)$	1446.0
$\omega_1(H_g)$	273.0		
$\omega_2(H_g)$	432.5	$\omega_1(H_u)$	342.5
$\omega_3(H_g)$	711.0	$\omega_2(H_u)$	563.0
$\omega_4(H_g)$	775.0	$\omega_3(H_u)$	696.0
$\omega_5(H_g)$	1101.0	$\omega_4(H_u)$	801.0
$\omega_6(H_g)$	1251.0	$\omega_5(H_u)$	1117.0
$\omega_7(H_g)$	1426.5	$\omega_6(H_u)$	1385.0
$\omega_8(H_g)$	1577.5	$\omega_7(H_u)$	1559.0

† Interpretation of an isotopically-induced line in the Raman spectra implies that this $\omega_6(G_g)$ mode should be at 1490 cm^{-1} [109].

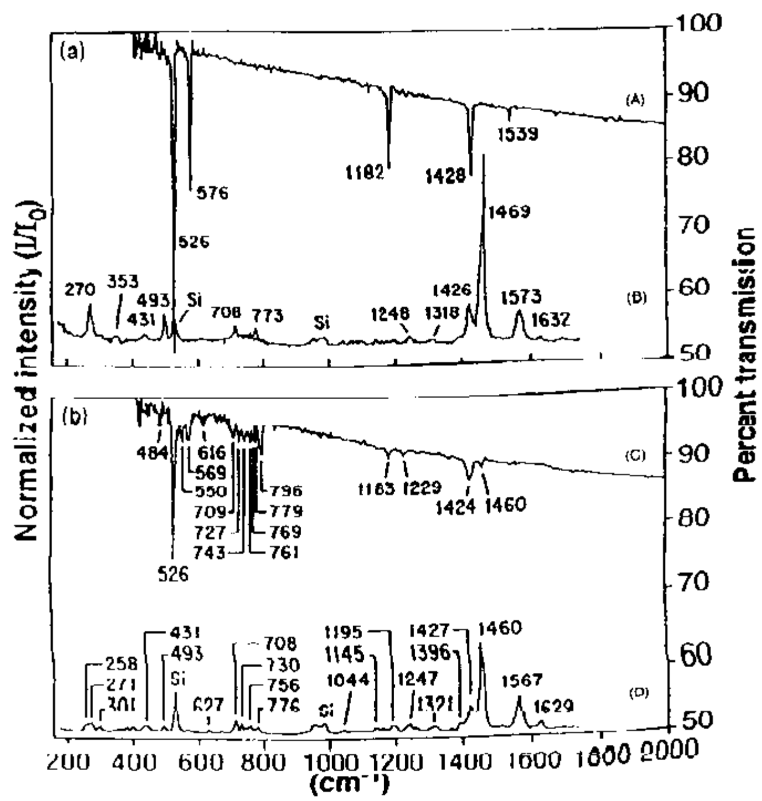

Figure 1-21: (a) Infrared (A) and Raman (B) spectra for C_{60} taken with low incident optical power levels (<50 mW/mm^2) to avoid photopolymerization. (b) Infrared (C) and Raman (D) spectra for C_{60} film subjected to intense optical power levels for several hours. Optical irradiation causes covalent bonding between the adjacent C_{60} molecules (see Sec. 1.3.2), thereby lowering the symmetry of the system, and giving rise to many more infrared and Raman lines in the spectra, as compared to pristine (unpolymerized) C_{60} films (a). [45].

1.7.1 Overview

To date, a variety of M/C_{60}/M (M = metal) rectifying diodes, field effect transistors (FETs), as well as photovoltaic and photorefractive devices have been proposed, and measurements have been carried out on a number of actual electronic devices. A few research groups have concentrated on applications based on the strong bonding at the C_{60}–Si interface [112, 113] and the incorporation of C_{60} into existing microfabrication processes. It has been demonstrated that C_{60} films can be patterned on silicon using conventional photoresist and liftoff techniques [114] achieving linewidths between 3 and 5 μm. Moreover, the C_{60} film itself can serve as a negative photoresist (decreasing solubility upon exposure to light) [115], yielding line resolution of better than 1 μm as shown below.

While a number of devices based on pristine C_{60} films have been investigated, the most promising electronic applications proposed to date utilize C_{60} in conjunction with selected conducting polymer composites. In this section, the structure and properties of C_{60}-based transistors (Sec. 1.7.2) and rectifying diodes (Sec. 1.7.3) are discussed, and C_{60}–semiconducting polymer heterojunctions are described for both rectifying diodes (Sec 1.7.4) and photovoltaic (Sec. 1.7.5) applications. This is followed by a variety of other electronics applications based on fullerenes.

It should be noted that most C_{60} devices are unstable in air due to the diffusion and photodiffusion of dioxygen [116, 117] into the large interstitial sites of the fullerene solid. Therefore, if C_{60}–polymer devices are to be commercialized, they need to be packaged in oxygen-resistant coatings. While such packaging is done routinely in the semiconductor industry, fullerenes are unique in that they themselves can be used to make oxygen-resistant seals [118].

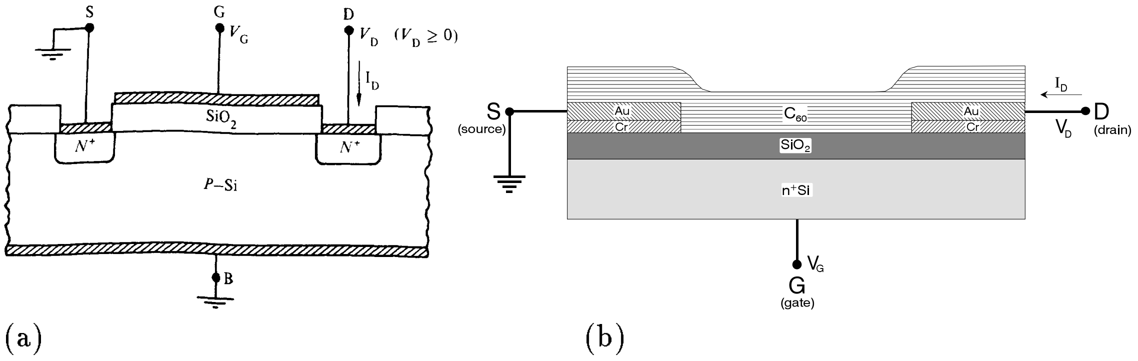

Figure 1-22: Cross-sectional view of field effect transistor (FET) structures: (a) the terminal designations and biasing conditions for conventional Si-based MOSFETs [119]. G, D, B, and S, respectively, denote the gate, drain, base, and source. (b) The corresponding structure for the fullerene (C_{60}) FET device [120].

1.7.2 C_{60} Transistors

In this subsection, field effect transistors based on C_{60} are described and are compared to their conventional silicon-based counterparts. The conventional silicon-based metal–oxide–semiconductor field effect transistor [MOSFET; see Fig. 1-22(a)] consists of two *p*–*n* junctions placed immediately adjacent to the region of the semiconductor controlled by the MOS gate. The carriers enter the structure through the source (S), leave through the drain (D), and are subject to the control by the bias voltage on the gate (G). The voltage applied to the gate relative to ground is V_G, while the drain voltage relative to ground is V_D. In this particular device geometry the source (S) and base (B) are grounded. As the gate voltage V_G is increased $V_G > V_T$, where V_T is the depletion-inversion transition-point voltage, an inversion layer containing mobile carriers is formed adjacent to the Si surface, creating a source-to-drain channel. Now, by keeping V_G fixed and varying V_D, the current–voltage characteristic I_D *vs.* V_D of the transistor can be determined for various gate voltages.

Fullerene-based *n*-channel FETs have been constructed [120–123] and an example of such a device is shown in Fig. 1-22(b). The corresponding current–voltage characteristics for this fullerene FET are shown in Fig. 1-23. In the fullerene FET

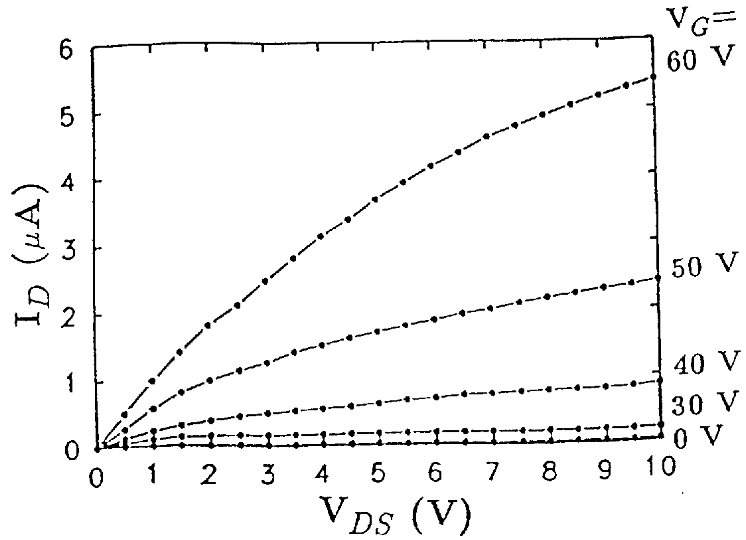

Figure 1-23: Room temperature drain current (I_D) *vs.* drain–source voltage (V_{DS}) characteristics at various gate voltages V_G (0, 30, 40, 50, 60 V) for a fullerene-derived field effect transistor with conduction in an n-type C_{60}/C_{70} channel induced at the SiO_2–C_{60} interface [120]. A schematic diagram for the device is shown in Fig. 1-22(b).

shown in Fig. 1-22(b), a highly doped n-type silicon wafer takes the place of the gate metal, a ~30–300 nm thick layer of SiO_2 serves as the oxide, and the fullerene film is the semiconductor. When an appropriate positive gate voltage V_G is applied (see Fig. 1-23), the drain current I_D increases, which indicates that a conduction channel is formed near the fullerene–insulator interface. The sign of the response indicates that the fullerene transistors are n-channel devices, consistent with C_{60} anion formation. Field effect mobilities of up to 0.08 cm^2/V·s were obtained from the I_D–V_D characteristics, which compares well with organic FETs, but is considerably lower than the carrier mobilities (0.5–1.0 cm^2/V·s) observed in C_{60} films by the Dember effect [124] and by the time-of-flight mobility measurements on C_{60} single crystals [125, 126]. This suggests that localized states at the SiO_2–C_{60} interface may play an important role in the electronic conduction.

Because C_{60}-based FETs operate as n-channel devices, they are subject to problems that are not experienced by the majority of organic materials investigated to date, which tend to be p-type. The field effect mobilities of 0.08 $cm^2/V{\cdot}s$ and the on–off ratios of $\sim 10^6$ are rapidly degraded by exposure to oxygen, presumably because charge transport in the C_{60} FETs depends on electron transport rather than on hole transport as is common in most organic materials-based FETs [123]. The fact that the device performance is not degraded by exposure to nitrogen gas [123] suggests that the oxygen molecules act as electron traps in the lattice of the C_{60} molecular solid (see also Sec. 4.4.2).

It was also found [123] that the treatment of the SiO_2 surface with TDAE (tetrakis-dimethylamino-ethylene) prior to deposition of the C_{60} film reduces the threshold voltage of the device, increases the mobility of the carriers in the C_{60} conduction channel, narrows the barrier width, and increases the band bending at the C_{60}–metal interface.

Overall, the electronic properties of C_{60} as a FET channel material show strong resemblance to amorphous semiconductors. The mobility of fullerene FETs may perhaps be improved by epitaxial growth of C_{60} on the surface or the use of Langmuir–Blodgett techniques, which could reduce the concentration of defect-induced traps.

1.7.3 C_{60}-Based Heterojunction Diodes

Of importance to many potential applications of fullerenes is the nature of the interface between fullerenes and various semiconductors and metallic substrates. Rectifying diodes have been demonstrated both for C_{60}–metal interfaces and for C_{60}–polymer heterostructures. Direct rectification between solid C_{60} and p-type crystalline Si has been demonstrated in Nb/C_{60}/p-Si and Ti/C_{60}/p-Si heterojunctions (as shown in Fig. 1-24) [127, 128].

Since the potential barriers at the Nb–C_{60} and Ti–C_{60} interfaces are close to zero [127], it has been concluded that it is the C_{60}/p-Si interface that is responsible for the strong rectifying properties of this heterostructure [127, 128]. Since the rec-

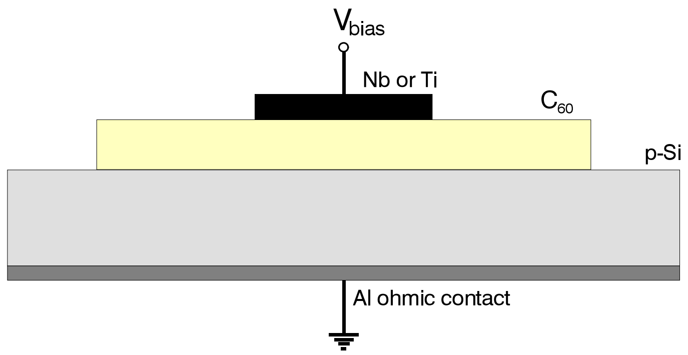

Figure 1-24: Schematic cross section of an Nb/C_{60}/*p*-Si structure used as a heterojunction diode. Rectification occurs at the C_{60}–Si interface [127].

tification occurs between the C_{60} and Si interfaces, and not between the C_{60}–metal interfaces, it is technically not proper to refer to these devices as Schottky diodes. Nevertheless, these heterojunctions were found to be strongly rectifying (by a factor of $\sim 10^4$ between $+2$ V and -2 V), and, as shown in Fig. 1-25, the sign of rectification is inverted when *n*-Si is used in place of *p*-Si. While rectifying behavior was observed in Al/AlO_x/C_{60}/Au devices [129], a different mechanism is responsible for rectification in this case, namely the tunneling of electrons through the AlO_x oxide layer, which is characteristic of the rectification behavior in metal–insulator–semiconductor (MIS) tunnel diodes. MIS devices with fullerenes as the active semiconductor contact were also studied by Pichler *et al.* [130].

1.7.4 C_{60}–Polymer Composite Heterojunction Rectifying Diode

Rectification behavior has also been demonstrated in C_{60}–polymer heterostructures, such as shown in Fig. 1-26(a) [131, 132]. Because of other optical experiments to be performed on these structures, a thin film transparent electrode, such as indium–tin oxide (ITO), is vacuum-deposited onto a glass substrate to form the lower transparent electrode. Next a thin film of polymer, such as a 1000 Å layer of methyl-ethyl-hydroxyl-polypropylvinyl (MEH-PPV) is spin-coated over the ITO, followed by a

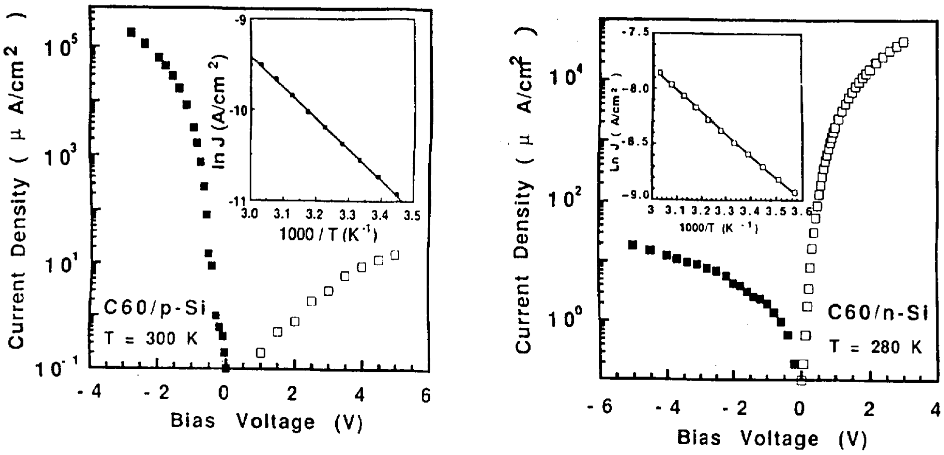

Figure 1-25: Room temperature current–voltage characteristics of C_{60}/p-Si and C_{60}/n-Si junctions with the filled squares for negative bias voltage and open squares for positive V. The complementary behavior between the junctions with n-Si and p-Si further supports the interpretation that it is the C_{60}–Si interfaces which yield efficient rectification and diode behavior in (Nb or Ti)/C_{60}/Si heterostructures. The insets, showing Arrhenius plots for each junction, yield activation energies (interpreted as barrier heights) of 0.30 eV for C_{60}/n-Si and 0.48 eV for C_{60}/p-Si [128].

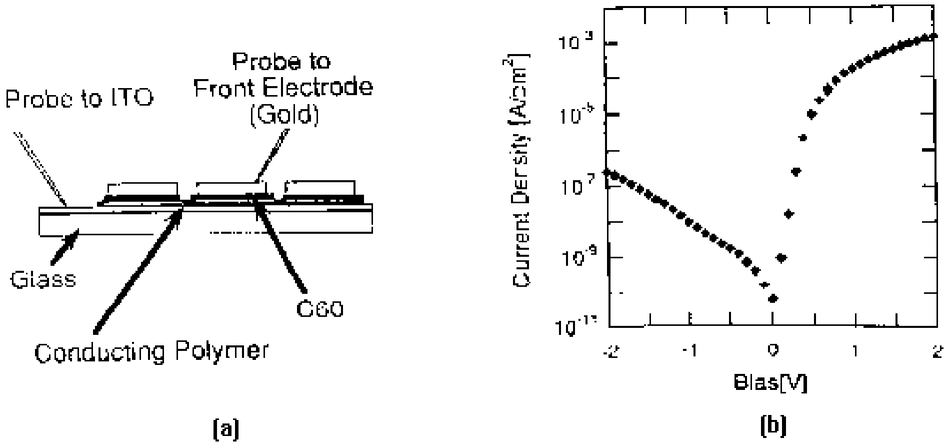

Figure 1-26: (a) ITO/polymer/C_{60}/Au heterojunction fabricated as a layered structure [132]. ITO denotes the optically transparent and electrically conducting indium–tin oxide. An example of a conducting polymer used in heterojunction applications is MEH–PPV. Light enters through the glass substrate and enters the device at the ITO electrode. (b) Dark current density *vs.* bias voltage showing rectification behavior in an ITO/MEH-PPV/C_{60}/Au device at room temperature [131].

vacuum-deposited C_{60} film of similar thickness. The active areas ($\sim$0.1 cm^2) of the device are defined by the Au or Al pads that are vacuum-deposited onto the upper C_{60} surface.

The I–V characteristics for such a C_{60}–polymer heterostructure diode are shown in Fig. 1-26(b) for a C_{60}/MEH-PPV heterojunction measured in the absence of light. Note that the current density is displayed on a log scale and that at ± 2 V bias voltage the rectification ratio is about four orders of magnitude, similar to the rectification behavior for the Nb/C_{60}/Si rectifying diodes discussed above that do not employ a C_{60}–polymer heterojunction. A positive voltage V implies that the ITO electrode is more positive than the metal electrode, so that the MEH-PPV polymer is positively biased with respect to the C_{60}. The forward current in Fig. 1-26(b) can be seen to exhibit a nearly exponential rise with applied bias voltage. Similar I–V measurements were made on Au/C_{60}/Au, Au/C_{60}/ITO, Au/MEH-PPV/Au, and Au/MEH-PPV/ITO layered structures, and all of these structures were found to

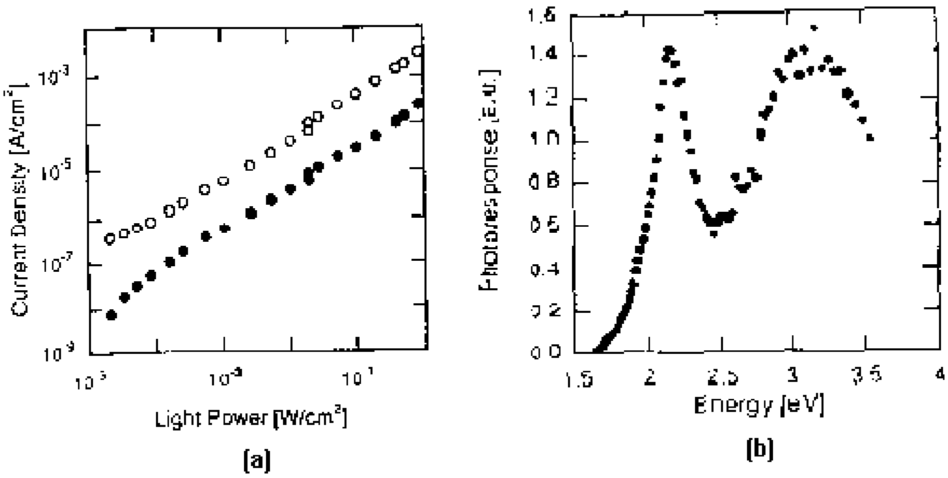

Figure 1-27: (a) Short-circuit current (closed circles) and photocurrent at −1 V bias (open circles) as a function of light intensity for the ITO/MEH-PPV/C_{60}/Au photovoltaic device. (b) Spectral response of the photocurrent in an ITO/MEH-PPV/C_{60}/Au photodiode at (reverse) −1 V bias [131].

exhibit ohmic (linear) I–V characteristics. It must therefore be concluded that the rectification occurs at the MEH-PPV/C_{60} interface [131].

1.7.5 C_{60}–Polymer Composite Heterojunction Photovoltaic Devices

C_{60}–polymer composite heterojunctions, such as the ITO/MEH-PPV/C_{60}/Al heterojunction shown in Fig. 1-26(a), have also been used to demonstrate photovoltaic behavior. In this context we show in Fig. 1-27(a) the short-circuit current density (closed circles with no applied bias voltage), and the photocurrent density (open circles with −1 V bias) as a function of the incident light flux on a log–log plot [131]. The open circuit (zero-current) voltage of the device under illumination was found to be ~0.5 V. Furthermore, this voltage was identified with the MEH-PPV/C_{60} junction, since such bias voltages applied to other junctions (e.g., C_{60}/Au and C_{60}/Al) did not affect the photoresponse. Both the short-circuit photocurrent and the biased-device photocurrent are reasonably linear over five decades of light intensity in the plot in Fig. 1-27(a), up to power densities approximately an order of magnitude greater than the terrestrial solar intensity level. The spectral dependence of the photocurrent (taken at -1 V bias) for an ITO/MEH-PPV/C_{60}/Au photovoltaic device is plotted in Fig. 1-27(b). The onset of the photocurrent near 1.7 eV matches the absorption edge for the MEH-PPV polymer, and the photoconductivity minimum near 2.5 eV matches the absorption maximum in the polymer. Since the light was incident from the polymer side of the polymer–C_{60} heterojunction [see Fig. 1-26(a)], it was concluded that the electron injection into the C_{60} must be from the polymer chains located very close to the heterojunction. Consistent with this experimental result, and using a charge carrier mobility of 10^{-4} cm^2/V-s for this device, an applied E-field of 10^5 V/cm, and a photocarrier lifetime of $\sim$1 ns [133], the distance a carrier could drift before recombination was estimated to be only a few angstroms.

Use of C_{60}–polymer heterojunctions for photovoltaic energy conversion device applications [131, 134] requires that the polymer be optimized for optical absorption at the peak of the solar spectrum, and the device must present a large effective area to the sunlight. C_{60}–polymer heterostructures appear promising for photovoltaic applications by further improving the materials and device design.

1.7.6 Microelectronic Fabrication and Photoresists

A number of advances have been made toward integrating fullerenes into the microfabrication processes for microelectronics. For instance, the use of fullerene films for patterning, as surfaces of uniform electric potential for electronics applications [135], for the pacification of surfaces [136], and as adhesives for direct bonding of the silicon wafers [113] have been suggested and are further discussed in this subsection.

The basis for patterning in microfabrication processes is the photochemical transformation that is induced by visible and ultraviolet (UV) light. In the absence of diatomic oxygen, solid C_{60} undergoes a photochemical transformation (see Sec. 1.3.2) when exposed to visible or ultraviolet light with photon energies greater than the optical absorption edge ($\sim$1.7 eV) [45, 84]. Phototransformation renders the C_{60} films insoluble in fullerene monomer solvents such as toluene, a property which may be exploitable in photoresist applications. Because the optical penetration depth in crystalline C_{60} in this spectral region is on the order of $\sim$0.1–1 μm, small particle size powders or thin films can undergo a significant fractional volume decrease upon phototransformation. The photochemical process is fairly efficient; a loss of 63% of the signature of monomeric units (i.e., van der Waals–bonded C_{60} molecules) is observed by Raman spectroscopy after the C_{60} film is exposed for $\sim$20 min to a modest light flux (20 mW/mm^2). Heating the transformed films to $\sim$100°C has been reported to return the system to the pristine monomeric state [137].

The patterning of micrometer-sized features on electronically compatible substrates has already been demonstrated using C_{60} on Si(100) [114]. The conventional photoresist and liftoff technique yielded lines of C_{60} with widths between 3 and 5 μm and heights of 0.4–0.8 μm [114]. This finding provides the opportunity to form many different structures using C_{60} films for a wide variety of applications, such as microelectronic devices, superconducting interconnects, and optical switching devices.

The C_{60} film itself can also serve as a negative photoresist (less soluble) [115] upon irradiation with ultraviolet light in vacuum. Such irradiation increases the cohesive energy in the fullerene solid substantially due to the presence of both molecular and reacted oxygen located at interstitial sites of the fcc C_{60} solid (see Sec. 4.4). The decreased solubility and lower vapor pressure of the phototransformed material enable wet (organic solvent) or dry (thermal or photoinduced sublimation) development of photodefined negative images, as shown on Fig. 1-28, where the sequence of steps in the photolithography process are shown schematically. The negative developing step shows that the C_{60} is retained on the Si substrate where it has been exposed to UV light. This photolithography process yields line resolution of better than 1 μm with good edge definition in the original Si substrate [138]. The efficiency of the

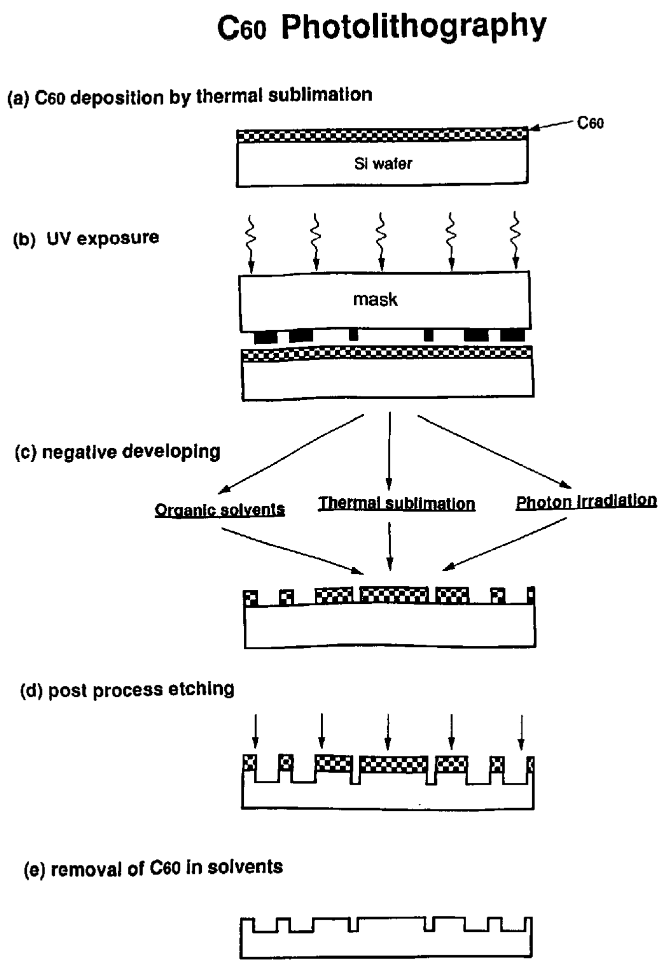

Figure 1-28: Sequence of steps (deposition, exposure, development, and pattern transfer) used in fullerene photolithography in which the C_{60} acts as a negative photoresist [138].

photolithography process can be greatly increased by exposing the C_{60} film to UV light in the presence of NO gas at ambient pressures [139], as discussed below.

Two methods, Raman scattering and chromatography, are typically used to monitor the photosensitivity of C_{60} as a photoresist, which is related to the degree of cross-linking of the C_{60} film. Raman scattering characterization shows a factor of 10^3 increase in photodimerization through introduction of NO gas at ambient pressures [139]. The enhanced photosensitivity of C_{60} in the presence of NO gas was confirmed by high-resolution chromatography characterization. The finding that amorphous carbon coatings can provide some protection for C_{60} films against the diffusion of oxygen and other species [118] could also be useful for photolithography applications.

In addition to photon beams, electron beams can be used to write patterns on C_{60} surfaces, either very fine lines on a nanometer scale using an STM tip operating at $\sim$3 eV, or thicker lines using an electron gun operating at $\sim$1500 eV [136]. This technology also appears promising for specific device applications.

1.7.7 Silicon Wafer Bonding

Utilizing the strong bonding between C_{60} and silicon at the C_{60}–Si interface, a thin layer ($\sim$600 Å) of C_{60} has been used as an adhesive to bond a 3 inch silicon wafer to another Si wafer at room temperature [113]. The thin C_{60} film between the two Si wafers was polycrystalline with grain sizes of $\sim$60 Å, while the Si wafer surface had a (100) orientation and was prepared as a hydrophilic surface. Some pressure was needed to bond the pair of wafers together. Interface energies of $\sim$40 erg/cm^2 and $\sim$20 erg/cm^2 were reported for the C_{60}–SiO_2 and C_{60}–Si interfaces and were measured by the crack length generated by inserting a razor blade at the bonding interface [113]. Examination of the debonded surfaces did not show adhering C_{60} layers, indicating a lower cohesive energy at the interface than between C_{60} molecules. It was also found that two C_{60}-covered Si wafers can easily be bonded to each other [113]. It was further speculated that a thin fullerene film could be used to bond selected smooth surfaces to one another or to bond a Si wafer to certain other smooth surfaces [140]. Since the strongest bonding is at the C_{60}–Si interface, a continuous single C_{60} monolayer would be expected to show bonding action to Si.

1.7.8 Fullerenes Used for Uniform Electric Potential Surfaces

For some electronics applications, surfaces with a uniform electrical potential are required. In the past, graphite and gold surfaces have been used to provide equipotential surfaces. It has been found that by applying a thin ($\sim$10 Å) deposit of germanium to a substrate (such as amorphous carbon, γ-irradiated NaCl or polished phosphorus bronze) and subsequently depositing an overlayer of $\sim$100 Å of fullerenes, a good equipotential surface is obtained [135]. The dangling bonds of the thin Ge interface layer would be expected to facilitate bonding to both the substrate and the fullerenes. Amorphous fullerene growth and uniform surface coverage of C_{60} on the Ge interface layer would be expected at room temperature, because of the low mobility and high sticking coefficient of the fullerenes to the Ge dangling bonds. The demonstration of this fullerene application was made with 85% C_{60} and 15% C_{70}. Fullerenes are useful for providing equipotential surfaces on metals because fullerenes are chemically stable and easy to deposit in vacuum [135].

1.7.9 Sensors

The possible use of C_{60} films as sensors for volatile polar gases such as NH_3 and tetrachloroethylene has been considered, exploiting the decrease in film resistance with gas adsorption and the resulting charge transfer. A linear dependence of the film resistance on gas concentration has been demonstrated as well as reversible and reproducible behavior on time scales of hours [141]. Sensitivity levels of a few ppm NH_3 in air have already been achieved, though many challenges remain before giving serious consideration to this potential application, including selectivity to the detection of specific gas species, response time (now on the order of seconds), sensitivity of the film calibration to humidity levels, stability of the sensor over longer times (days), and cost/performance comparison with alternative sensors for the same gas.

1.7.10 Nanotechnology

Nanotechnology is a new, potent field on the crossroads of physics, engineering, and material science, which searches for ways to directly manipulate atoms and molecules to build new materials and molecular devices. One might describe nanotechnology as the physicists' answer to genetic engineering. While a biologist might manipulate single genes to modify a cell in a desired way, the physicist might manipulate a single molecule to build a device with desired characteristics. The ultimate feat of nanotechnology would be to fashion intelligent (logic) devices from plain matter that, by itself, possesses no intelligence of its own.

At the American Physical Society's 1959 annual meeting at the California Institute of Technology, Richard Feynman, the legendary physicist, delivered his landmark address entitled "There's Plenty of Room at the Bottom" [142] that started out the nanotechnology revolution. In his talk, Feynman suggested the possibility of creating new materials by mechanically assembling molecules, *an atom at a time.* Following Feynman's lead, other scientists delved into the field. Working independently, von Hippel predicted [143] dramatic material science possibilities if new advances in "molecular designing" and "molecular engineering" of materials could be achieved. After the basic concept of nanotechnology was proposed in 1974 by Toniguchi in Japan, the nanoscale fabrication principles were further advanced by Drexler [144–146] and many others.

Fullerenes, particularly C_{60}, are perhaps perfect for materials manipulations on the molecular scale, including the forming and tailoring of molecular size structures. The C_{60} molecules are quite inert, nearly spherical, and nonpolar due to symmetry,

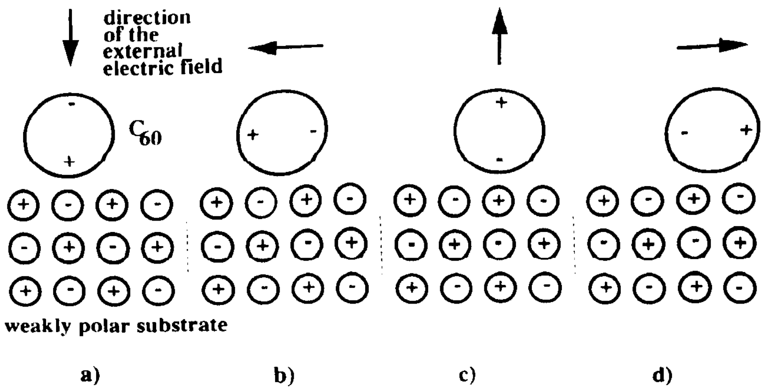

Figure 1-29: The principle of moving C_{60} molecules by a rotating external electric field. An isolated molecule is assumed to be adsorbed on an ideally flat, weakly polar substrate. A rotating external electric field induces a dipole moment that exceeds the effect of the substrate dipoles on the molecule; the successive directions of the field are shown in (a) through (d). The large diameter of the molecule should allow coupling to successive poles, thereby generating lateral movement [148].

their size is very large, the van der Waals bonds between the individual molecules are weak, and thin fullerene films can be grown easily. A C_{60} molecule can be compared to a huge atom, and it is, therefore, possible to manipulate such molecules using the same techniques that have been developed for the manipulation of noble gas atoms using STM probe tips [147]. Moreover, some other manipulation methods may be possible for C_{60} that are not possible for any other species. For instance, it has been proposed [148] that a C_{60} molecule can be "rolled" (diffused) along the surface of a suitable ionic substrate by a rotating external electric field, utilizing the large size and polarizability of C_{60} as illustrated in Fig. 1-29. A recent tribological study [149] suggested that nanocrystalline C_{60} islands grown on certain types of substrates [e.g., NaCl(011)] could be used as transport devices for fabrication processes of nanometer-sized machines. These 0.5–3 ML C_{60} islands might play the role of a tiny "nanosled" transporting larger molecules (e.g., biomolecules) to a desired location [149].

Since fullerenes are all-carbon molecules and have been shown to be of interest for biotechnology applications (from drug delivery to the treatment of AIDS [150, 151]), fullerene-based nanodevices may be capable of biological interfacing. Nanoscale fabrication of logic information devices capable of such interfacing should enable construction of valuable nanoscale robots, sensors, and machines.

To interconnect these nanoscale devices, it may someday be possible to utilize carbon nanotubes for nanowire applications. By varying the chirality and diameter of carbon nanotubes, it should be possible to alter their properties from metallic to semiconducting to insulating. Such nanotubes could, in their own right, lead to nanoscopic electronic devices based on concentric semiconducting and metallic carbon tubules as shown in Fig. 1-30. The significance of carbon nanotubes as electronic materials is the demonstration of quasi-1D cylindrical wires with a large aspect (length-to-diameter) ratio, thereby opening a new field of 1D physics for the study of 1D cylindrical wires or hollow tubes. There is also the possibility of the application of such filled nanotubes with regard to low-dimensional transport, magnetism, and superconductivity. The heterostructures shown in Fig. 1-30 could function as an insulation-clad metallic wire, a tunnel junction, a capacitor in memory devices, or a transistor in switching circuitry [152, 153]. Because the tubes do not require any doping by impurities, as conventional semiconductors do, but acquire their electronic properties from their geometry, the resulting devices should be highly thermally stable and have high intrinsic mobility. Schematics for several devices have been suggested (see Fig. 1-30). To facilitate such applications, the mechanical and electronic properties of a free-standing carbon nanowire have been measured [154]. By employing the low-energy electron projection microscope for *in situ* visual control, it was possible to attach or detach a fine manipulating tip to or from a carbon fiber network. In this way it was possible to apply an electrical potential to a single nanometer-sized fiber while observing the electron projection images at TV sampling rates. The maximum current passed through individual free-standing wires of diameter $\sim$10 nm and lengths $\sim$1 μm exceeded a current density of 10^6 A cm^{-2} at room temperature [154].

An alternative method of constructing an ultrathin wire involves filling the hollow

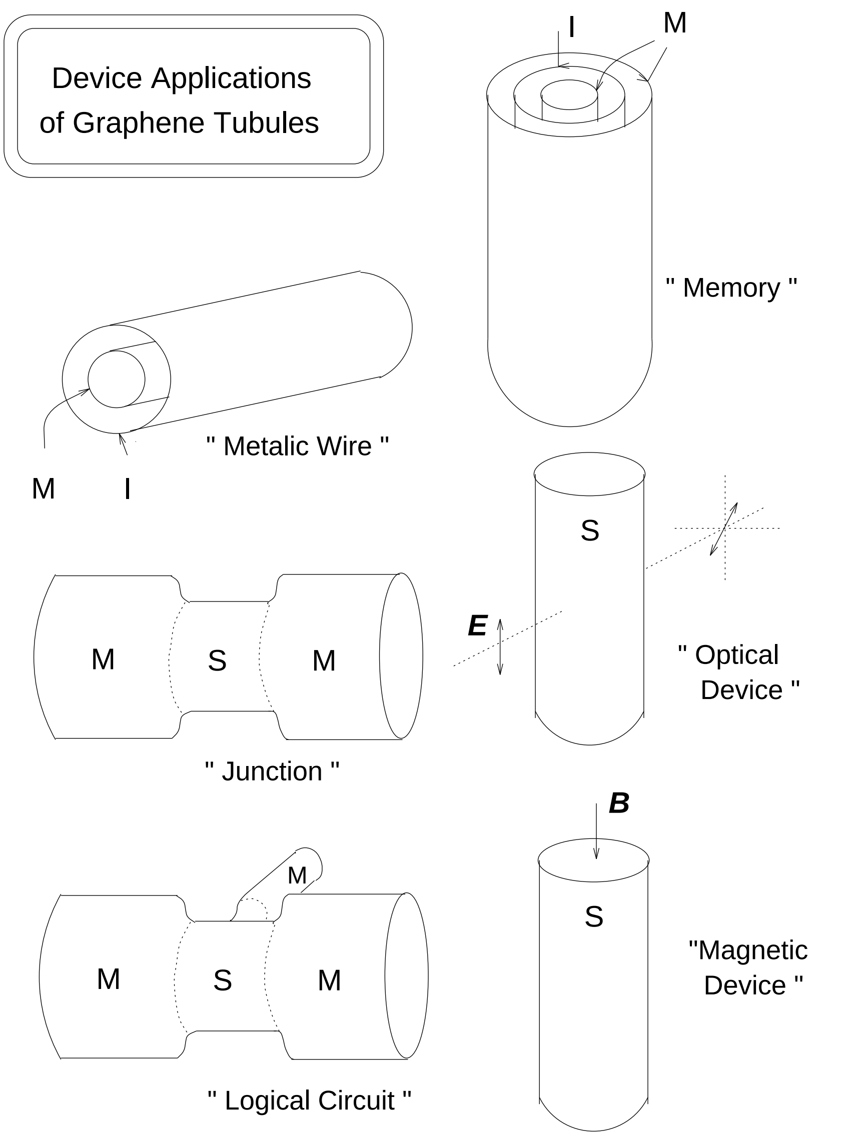

Figure 1-30: Schematic presentation of several proposed electronic device applications for carbon nanotubes [23].

cavity of the nanotubes (which are large enough in diameter to contain atoms of any element in the periodic table) with metallic atoms arranged much like "peas in a pod" [155, 156]. Although the lengths of the filled nanowires thus far produced are impractically short [156], the use of carbon nanotubes as 1D quantum wires merits further attention.

While the field of nanotechnology is still about halfway between science and science fiction, it is a very active fast-growing field whose promise of nanoscale molecular devices and orders of magnitude increase in the integration density of electronic components is too appealing to be ignored. The discovery of fullerenes has given a significant boost to the field of nanotechnology by providing an abundance of stable, identical, highly symmetric, nonreactive, and relatively large molecules that can, in principle, be manipulated one at a time. Fullerenes at semiconductor interfaces can be utilized to modify electronic device behavior on nanometer length scales. In such applications, C_{60} anions alone represent an almost ideal spherical capacitor that can store charge. Together with other carbon structures, such as tubules (serving as nanowires), a new carbon-based nanotechnology can be envisioned.

1.7.11 Commercialization and Patents

It was not until after 1990, when fullerenes were first synthesized in macroscopic quantities [7], that the unique physical, chemical, and biological properties of fullerenes were fully appreciated, and fullerenes were used to build some prototype devices. Fullerenes, therefore, now appear ripe for commercial exploitation. Indeed, suggested fullerene uses have become a hot topic at the U.S. Patent Office [157].

Table 1.4 summarizes a wide range of possible practical fullerene applications for which a patent has been granted or a patent application has been disclosed. As suggested by the great number of polymer-related patents, it seems likely that the use of C_{60} and other fullerenes as building blocks for new chemicals will be a very important future application. Rechargeable batteries may turn out to be another promising application, due to the fact that reversible attachment of hydrogen to C_{60} could provide a charge storage per unit mass that is better than current metal hydride battery technology [158]. Somewhat similar considerations apply to hydrogen storage, perhaps for vehicle propulsion. Use of fullerenes for conversion to other solid products, such as diamond or SiC, may be of value in the future. As a component of solid fuel rocket propellant, fullerenes or fullerene soot may have practical advantages. Fullerenes as optical limiters and as a component in chromatography columns appear to be small-scale applications already under consideration [158].

One of the largest impediments to the large-scale commercialization of fullerenes is their relatively high cost. Although the price has come down from about \$1000–\$2500 per gram for mixed fullerenes in 1990 to less than \$100 per gram for 99% pure C_{60} today, this is still prohibitively expensive for most commercial applications (e.g., batteries). This cost is bound to decrease further, however, since new methods of synthesis, production, purification, separation, processing, and deposition of various fullerenes and their numerous compounds are constantly being discovered. Recently, a joint venture company, Fullerene Technologies Inc., was formed by Mitsubishi and MER (Tucson, Arizona) to explore the commercialization of fullerene-based batteries and hydrogen-storage devices. This joint venture announced plans for a plant having a fullerene production capacity of a few tons per day [159]. Other companies actively working on fullerene commercialization include such giants as Exxon (fullerene precursors), duPont (fullerene-based compounds), Xerox (fullerene inks, toners, developers, and photoreceptors), SRI (fullerene catalysts, electronics, and fibers), NEC (fullerene-based polymers), and AT&T (fullerene photoconductors, superconductors, and photolithography) [160, 161].

Table 1.4: Some uses of fullerenes suggested by patents and patent applications.

Use	Patent[a]
Electronic applications	
Carbon films	JP 06184738
Electrophoretic display	JP 06148693 A2
Bilayer resist-coated substrate	JP 06061138 A2
Tunnel diode	JP 06029556 A2
Photolithography, photopolymer	US 08-037056 A, US 08-073533 A
Double layer capacitor and storage device	US 5319518
Atomic scale electronic switch	US 5323376
Conductive compounds	US 5391323, US 5380595
Superconductors	US 5294600, US 5325002, US 5332723, US 5380703, US 5356872, US 5348936
Optical applications	
Electrophotographic imaging	WO 9308509 A1, US 5215841, JP 06222575 A2, JP 05289381 A2, JP 05088387 A2, US 5215841, US 5178980, JP 6-298532 A, JP 7-1546 A
Sensitizer of a photorefractive polymer	US 5361148
Solar cells from fullerenes	JP 06244440 A2
Electroluminescent cell	JP 05331458 A2
Magneto-optical recording	JP 06002106 A2
Optical limiters (flash goggles)	US 5172278, US 5325227
Nonlinear optical thin films	JP 5-142597
Photoelectronic devices	WO 9405045, US 5171373, US 5331183
Materials applications	
Oriented diamond film	WO 9426953 A1
Nucleating diamond growth	WO 9305207 A1
Diamond-like carbon coating	US 5393572
Conversion of fullerenes to diamond	US 5209916, US 5273788, JP 05305227 A2, US 5308661, US 5328676, US 5360477, US 5370855
Sensors	
NO_x detector	JP 06186195 A2
Sensor for analyses in fluid media	DE 4241438 A1, US 5334351
Gas, temperature, particle sensor	JP 06118042, JP 5-099759, DE 4142959
Detection of organic vapors	US 5395589
Biological and medical applications	
Fullerene-coated surfaces and cell culture	WO 9400552 A1
Diagnostic and/or therapeutic agents	WO 9315768 A1
Biologically active material	JP 3-94692
Magnetic resonance imaging	WO 9303771 A1

Table 1.4: CONTINUED: Some uses of fullerenes suggested by patents and patent applications.

Use	Patent[a]
Chemicals	
Selective functionalization of fullerenes on molecular sieves	US 5364993
Synthesis of derivatized fullerenes	EP 546718 A2
Lubricants	JP 05179269 A2, US 5374463
Lubricants and adhesives	US 5382718, US 5382719, US 5354926
Charge transfer complexes	WO 9302012 A1
Polysubstituted fullerenes	US 5166248
Liquid ink compositions	US 5114477, US 5322756
Surface coating	US 5120669, US 5368890
Cosmetics	JP 5-17327, JP 5-17328
Catalyst	US 5336828, US 5347024
H_2O_2 production	US 5376353
Polymer chemistry and technology	
Fullerene–diamine adducts	DE 4229979 A1
Fullerene-grafted additives to lube oil	US 5292444
Grafted polymers	US 5292813
Anionically polymerized C_{60}–polymers	US 5270394
Modified viscoelastic polymer properties	EP 544513 A1
Electrochemical applications	
Secondary battery	JP 05101850 A2
Li secondary batteries	JP 07006764 A2, JP 05275078 A2, US 5302474, JP 05082132 A2, JP 05275083 A2
Nonaqueous batteries	JP 05325974 A2, JP 0531477 A2
Fuel cell electrodes	WO 9422176 A1, US 5277996, JP 05229966 A2, JP 527801 A2
Other applications	
Storage of nuclear materials	US 5350569
Solid-state rocket fuel	US 5341639
Ballistic missile shield	US 4922827
Metallurgy (additives to steel alloys)	US 5288342
Identification tracer in fuels	US 5234475
Electromagnetic shielding resin	JP 5124894

[a] US = United States patent; JP = Japanese; FR = French; DE = German; WO = International patent application; EP = European patent application.